IMMUNOLOGY

Aging-associated deficit in CCR7 is linked to worsened glymphatic function, cognition, neuroinflammation, and β-amyloid pathology

Sandro Da Mesquita[1]*†‡, Jasmin Herz[2,3]†, Morgan Wall[1], Taitea Dykstra[2,3], Kalil Alves de Lima[2,3], Geoffrey T. Norris[4], Nisha Dabhi[1], Tatiana Kennedy[1], Wendy Baker[1], Jonathan Kipnis[1,2,3]*

Aging leads to a progressive deterioration of meningeal lymphatics and peripheral immunity, which may accelerate cognitive decline. We hypothesized that an age-related reduction in C-C chemokine receptor type 7 (CCR7)–dependent egress of immune cells through the lymphatic vasculature mediates some aspects of brain aging and potentially exacerbates cognitive decline and Alzheimer's disease–like brain β-amyloid (Aβ) pathology. We report a reduction in CCR7 expression by meningeal T cells in old mice that is linked to increased effector and regulatory T cells. Hematopoietic CCR7 deficiency mimicked the aging-associated changes in meningeal T cells and led to reduced glymphatic influx and cognitive impairment. Deletion of CCR7 in 5xFAD transgenic mice resulted in deleterious neurovascular and microglial activation, along with increased Aβ deposition in the brain. Treating old mice with anti-CD25 antibodies alleviated the exacerbated meningeal regulatory T cell response and improved cognitive function, highlighting the therapeutic potential of modulating meningeal immunity to fine-tune brain function in aging and in neurodegenerative diseases.

INTRODUCTION

Aging-related neurological disorders are rapidly becoming a major financial burden on health care worldwide. Alzheimer's disease (AD) is the most prevalent aging-associated dementia, accounting for 60 to 80% of all dementia cases and affecting close to half of the elderly population over the age of 85 (*1*, *2*). AD is characterized by severe behavioral deficits, particularly in cognitive faculties, whose underlying pathophysiological mechanisms are poorly understood and lack effective treatments (*3*–*5*). Accumulating evidence over the past decade has shown a close association between changes in neuroimmune-related mechanisms and the etiology and progression of AD (*6*–*11*). Microglia, the brain-resident immune cells, have been extensively studied and seem to play a central role in modulating AD pathology (*11*–*15*). Less attention has been focused, however, on changes in the adaptive immune response at the brain-meningeal border in aging and in AD.

The meninges, which ensheath the brain, comprise a unique neuroimmune interface, harboring a diverse immune cell population that plays an essential role in maintaining brain homeostasis (*16*–*18*) and in fine-tuning processes such as neuroinflammation, tissue repair, and neuronal activity (*19*–*25*). Notably, different behavioral aspects such as cognition, sociability, and anxiety are modulated by meningeal T cell–derived cytokines that signal directly to their cognate receptors expressed on neurons (*19*, *22*, *25*). The brain meninges also harbor bona fide lymphatic vessels that constantly drain molecular solutes from the cerebrospinal fluid (CSF) into the cervical lymph nodes (*23*, *26*, *27*). Aging in mice was recently shown to induce a deleterious loss of meningeal lymphatic coverage and drainage capacity, which is closely associated with cognitive decline (*28*). Ablation of the meningeal lymphatic vasculature in adult mice resulted in deficient clearance of brain solutes through the glymphatic system, as well as cognitive impairment and accumulation of β-amyloid (Aβ) in the brains of familial AD transgenic mice (*28*). Besides draining CSF, the lymphatic vasculature also regulates the immune response in the brain meninges (*17*, *23*). Notably, it was shown that meningeal immune cell egress is mediated by C-C chemokine receptor type 7 (CCR7) expression and that ablation of meningeal lymphatic vessels in a model of neuroinflammation results in altered activation of T cells in the cervical lymph nodes (*23*).

Aging induces marked changes in the immune system (*18*, *29*, *30*). Moreover, the role of adaptive immune cells in AD was emphasized by reports showing altered AD-related Aβ brain pathology in immunodeficient mouse models (*31*, *32*). Little is known, however, about the effects of aging on meningeal immunity and whether changes in meningeal immunity underlie the observed deficient clearance of brain waste and the build-up of Aβ in AD (*17*, *18*, *33*, *34*). Here, in exploring the meningeal immune profiles of old mice, we observed a reduction in CCR7 expression by T cells. To investigate a potential link between this decreased CCR7 expression in immune cells and brain dysfunction, we examined the changes in meningeal immunity, cognition, glymphatic function, and brain single-cell transcriptomic profile in CCR7-deficient mice. We also provide evidence showing that decreased CCR7 expression affects brain Aβ pathology and cognitive function in a mouse model of familial AD and that normalization of the exacerbated regulatory T cells (T_{regs}) in the aged meninges correlates with a better cognitive performance.

RESULTS

Meninges of old mice encompass more FOXP3$^+$ T_{regs} and fewer CCR7-expressing T cells

Aging has a profound impact on immune cells of both the peripheral and the central nervous systems (*14*, *18*, *30*). Our flow cytometric

---

[1] Department of Neuroscience, Center for Brain Immunology and Glia (BIG), University of Virginia, Charlottesville, VA, USA. [2] Center for Brain Immunology and Glia (BIG), Washington University in St. Louis, St. Louis, MO, USA. [3] Department of Pathology and Immunology, School of Medicine, Washington University in St. Louis, St. Louis, MO, USA. [4] Department of Immunology, University of Washington, Seattle, WA 98109, USA.

*Corresponding author. Email: damesquita@mayo.edu (S.D.M.); kipnis@wustl.edu (J.K.)

†These authors contributed equally to this work.

‡Present address: Department of Neuroscience, Mayo Clinic, Jacksonville, FL, USA.

analysis of the T cell response in mouse meningeal preparations (composed mostly of dural and arachnoid layers) revealed a significantly larger number of T cells ($NK1.1^-TCR\beta^+$) in old mice (24 to 25 months of age) than in adult (2 to 3-month-old) mice (Fig. 1, A to C), confirming previously published findings (*14*). Assessment of forkhead box P3 (FOXP3) expression by meningeal leukocytes revealed a significant increase in the frequency and number of $CD4^+FOXP3^+$ T_{regs} in the old mice (Fig. 1D and fig. S1A). Assessment of the brain-draining deep cervical lymph nodes (dCLNs) revealed decreased frequency of T cells and an increase in frequency of the T_{regs} in old mice (Fig. 1, E to H). Together, this translated into an overall significant decrease in the number of $CD4^+FOXP3^-$ effector T cells (fig. S1B). Analysis of blood and liver samples revealed no differences in total $CD45^+$ cells or in $CD4^+FOXP3^+$ T_{regs} between adult and old mice (fig. S1, C to J).

We have previously shown that impaired signaling through CCR7 results in accumulation of T cells in the brain meninges (*23*). To find out whether altered CCR7 expression could explain the

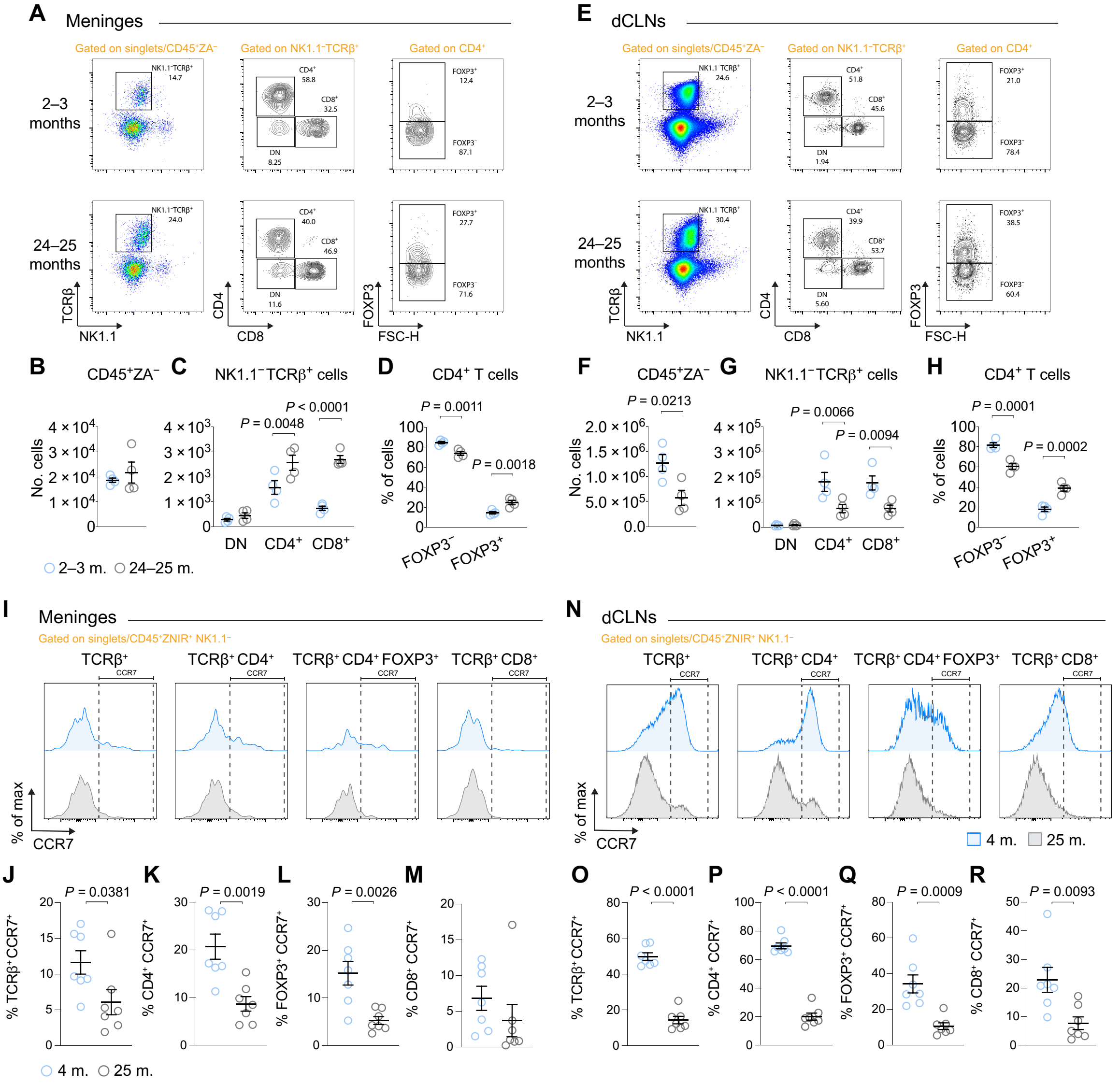

Fig. 1. Aging leads to abnormal T_{reg} response and reduced $CCR7^+$ T cell frequency in the brain meninges and draining lymph nodes. (**A**) Representative flow cytometry dot and contour plots showing the gating strategies used to determine $NK1.1^-TCR\beta^+$ cells, $CD4^+$, $CD8^+$, DN T cells, and $FOXP3^-$ or $FOXP3^+$ CD4 T cells in the meninges of mice at 2 to 3 or 24 to 25 months (m.). (**B** to **D**) Graphs with quantification of (B) $CD45^+ZA^-$ cell numbers; (C) DN, $CD4^+$, and $CD8^+$ T cell numbers; and (D) frequency of $FOXP3^-$ or $FOXP3^+$ (percentage of $CD4^+$ T cells) in the meninges. (**E**) Representative flow cytometry dot and contour plots showing the gating strategies used to determine the subpopulations of T cells in the dCLNs. (**F** to **H**) Graphs with quantification of (F) $CD45^+ZA^-$ cell numbers; (G) DN, $CD4^+$, and $CD8^+$ T cell numbers; and (H) frequency of $CD4^+FOXP3^-$ or $CD4^+FOXP3^+$ in the dCLNs. Data are presented as means ± SEM; $n = 4$ per group; two-tailed unpaired Student's *t* test in (B) and (F); two-way analysis of variance (ANOVA) with Sidak's multiple comparisons test in (C), (D), (G), and (H); representative of two independent experiments. (**I**) Representative histograms of $CCR7^+$ cells in the meninges at 4 or 25 months of age. (**J** to **M**) Frequencies of CCR7-expressing (J) $TCR\beta^+$, (K) $CD4^+$, (L) $CD4^+FOXP3^+$, and (M) $CD8^+$ T cells in the meninges. (**N**) Representative histograms of $CCR7^+$ cells in the dCLNs at 4 or 25 months of age. (**O** to **R**) Frequencies of CCR7-expressing (O) $TCR\beta^+$, (P) $CD4^+$, (Q) $CD4^+FOXP3^+$, and (R) $CD8^+$ T cells in the dCLNs. Data are presented as means ± SEM; $n = 7$ per group; two-tailed unpaired Student's *t* test; representative of two independent experiments. FSC-H, forward scatter-height.

increase in T cell numbers observed in the meninges of old mice, we performed direct ex vivo staining of CCR7 (fig. S1K) on meningeal immune cells from mice at the ages of 4 months (adult) and 25 months (old). A smaller proportion of CCR7-expressing T cells, including $CD4^+FOXP3^+CCR7^+$ T_{regs}, was observed in meninges of the old mice than of the adult mice (Fig. 1, I to M, and fig. S1, L to O). Decreased proportions of CCR7-expressing effector T cells and T_{regs} were also observed in the dCLNs of old mice (Fig. 1, N to R, and fig. S1, P to S). These data indicate that old mice exhibit T cell accumulation in the meninges and decreased T cell retention in the dCLNs, possibly owing to their lack of CCR7 and their impaired migration capacity.

Next, we used $CCR7^{GFP}$ reporter mice to evaluate CCR7 expression levels in adult (3-month-old) and middle-aged (12- to 14-month-old) mice. Analysis of the brain cortex, choroid plexus, and meninges of adult $CCR7^{GFP}$ reporter mice by flow cytometry (fig. S2, A to C) showed that most of the brain-associated $CCR7^{high}$ leukocytes are predominantly found in the meninges (fig. S2B). Moreover, a significantly higher frequency of $CCR7^{high}$ leukocytes was observed in the dCLNs than in the blood and liver (fig. S2C), again underscoring the importance of CCR7 as a mediator of leukocyte egress through lymphatic vessels from the meninges into the dCLNs. We also found that most of the $CCR7^{high}$ leukocytes in the meninges were also T cell receptor β–positive ($TCR\beta^+$; ~83% of total $CD45^+CCR7^{high}$; fig. S2, D and E) and that ~27% of meningeal $CD4^+CD25^+$ T cells expressed high levels of CCR7 (fig. S2F). Approximately 96% of $CCR7^{high}$ leukocytes in the dCLNs and 95% in the blood were $TCR\beta^+$ (fig. S2, D and E), and more than half of the $CD4^+CD25^+$ T cells in the dCLNs expressed high levels of CCR7 (fig. S2F). Thus, consistent with our ex vivo staining data, the middle-aged $CCR7^{GFP}$ reporter mice showed a significant decrease in CCR7-expressing $TCR\beta^+$ T cells, relative to their adult counterparts in the meninges and dCLNs (fig. S2, G and H), but not in the blood or liver (fig. S2, I and J).

Together, these results point to a heightened T_{reg} response in the brain meninges and draining dCLNs of old mice, with concomitant reduction in $CCR7^{high}$ T cells. In line with our data, previous studies have reported an increased frequency of $CD4^+FOXP3^+$ T_{regs} in the spleen and peripheral lymph nodes of old mice relative to their younger counterparts (*35*).

CCR7 deficiency boosts meningeal T_{regs} in adult mice

To find out whether a decrease in CCR7 expression in the hematopoietic compartment would mimic the observed aging-related effects on meningeal immunity, we irradiated adult wild-type (WT) mice (while covering their heads with a lead shield to preserve brain-resident immune cells) and then carried out adoptive transfer of bone marrow cells isolated from WT or CCR7-deficient ($CCR7^{-/-}$) donor mice (see fig. S3A for more experimental details). As observed earlier in old mice, mice that received $CCR7^{-/-}$ bone marrow also showed increased numbers of $CD4^+$ (and $CD8^+$) T cells in the meninges (Fig. 2, A to C). Conversely, these cell numbers were decreased in the dCLNs (Fig. 2, D to F), as well as in the superficial CLNs, inguinal lymph nodes, and spleen (fig. S3, B to J), upon $CCR7^{-/-}$ bone marrow transplantation (BMT).

We next used cytometry by time of flight (CyTOF) to further examine the changes in meningeal immunity induced in 5-month-old mice by CCR7 deficiency. Analysis of differential marker expression in meningeal leukocytes ($CD45^+$ live singlets) using Rphenograph enabled us to identify 21 clusters (and a cluster of undefined cells; Fig. 2G and fig. S4A), of which only cells of the CD4 and CD8 clusters were significantly increased in $CCR7^{-/-}$ mice (Fig. 2H). This increased number of meningeal T cells in the $CCR7^{-/-}$ group was associated with a decrease in the number of cells in the macrophage 2 cluster (Fig. 2H). Upon closer analysis of activation markers and transcription factor expression on cells from the three identified $CD3^+TCR\beta^+$ T cell clusters (CD4, CD8, and double-negative T cells; fig. S4B), we observed an increased frequency of $CD8^+$T-bet^{low} T cells and of $CD4^+FOXP3^+$ T_{regs} in the meninges of $CCR7^{-/-}$ mice (Fig. 2, I and J). The increased frequency of meningeal T_{regs} in the $CCR7^{-/-}$ group was accompanied by a decrease in all T-bet^{high} T cell subclusters (Fig. 2, I and J). Flow cytometric analysis of ex vivo–stimulated meningeal T cells confirmed the increase in frequency of $CD4^+FOXP3^+$ T_{regs} in $CCR7^{-/-}$ mice and a concomitant decrease in frequency of interferon-γ (IFN-γ)–producing CD4 T cells (fig. S4, C to F). Both CD4 and CD8 meningeal T cells from the $CCR7^{-/-}$ group showed a trend toward decreased IFN-γ production relative to the WT control (fig. S4, G to I). The increase in T_{regs} in the $CCR7^{-/-}$ group was evident in the meninges and dCLNs but was only minor in the liver and was not detected in the blood (fig. S5). Together, these results show that CCR7 deficiency (either constitutive or upon BMT) leads to an aging-like dysregulated T cell response, characterized by decreased T-bet^{high} and IFN-γ–producing CD4 T cells and an abnormal increase in T_{regs} in the brain meninges and dCLNs.

Hematopoietic CCR7 deficiency hinders spatial memory and glymphatic function

T cells participate in the modulation of neuronal activity and higher cognitive functions (*19*, *22*, *25*, *36*). In view of the abnormal T cell response due to CCR7 deficiency, we compared the performance of 5- to 7-month-old $CCR7^{-/-}$ mice and their age-matched WT littermates in different behavioral tests. In the open-field test, both groups showed comparable values in terms of total distance traveled, velocity, and time spent in the center of the arena, which indicated similar exploratory activity and anxiety-like behavior (fig. S6, A to C). Equivalent performances in the open field were also observed after (WT or $CCR7^{-/-}$) BMT (fig. S6, D to F). However, both $CCR7^{-/-}$ mice (Fig. 3, A to E) and WT mice that had received $CCR7^{-/-}$ bone marrow (at 4 months of age; Fig. 3, F to J) performed worse in the novel location recognition and Morris water maze (MWM) tests than their respective controls. These results are in line with previously reported learning deficits displayed by $CCR7^{-/-}$ mice in the Barnes maze test (*37*), reinforcing the notion that impaired CCR7-dependent immune cell egress is associated with worse cognitive function.

Reduced meningeal lymphatic drainage has been linked to both aging-related cognitive decline and impaired recirculation of CSF through the brain via the glymphatic system (*28*). On the basis of that finding, we next examined whether the abnormal immune response observed in $CCR7^{-/-}$ mice is correlated with glymphatic dysfunction. To our surprise, 5- to 7-month-old $CCR7^{-/-}$ mice showed significantly reduced glymphatic influx of molecular tracers from the CSF into the brain (Fig. 3, K and L), even when the meningeal lymphatic vasculature was both morphologically and functionally intact (fig. S6, G to J). Reduced glymphatic function can be attributed to deficits in aquaporin 4 (AQP4) at the astrocytic endfeet (*38*, *39*). In attempting to provide a possible explanation for

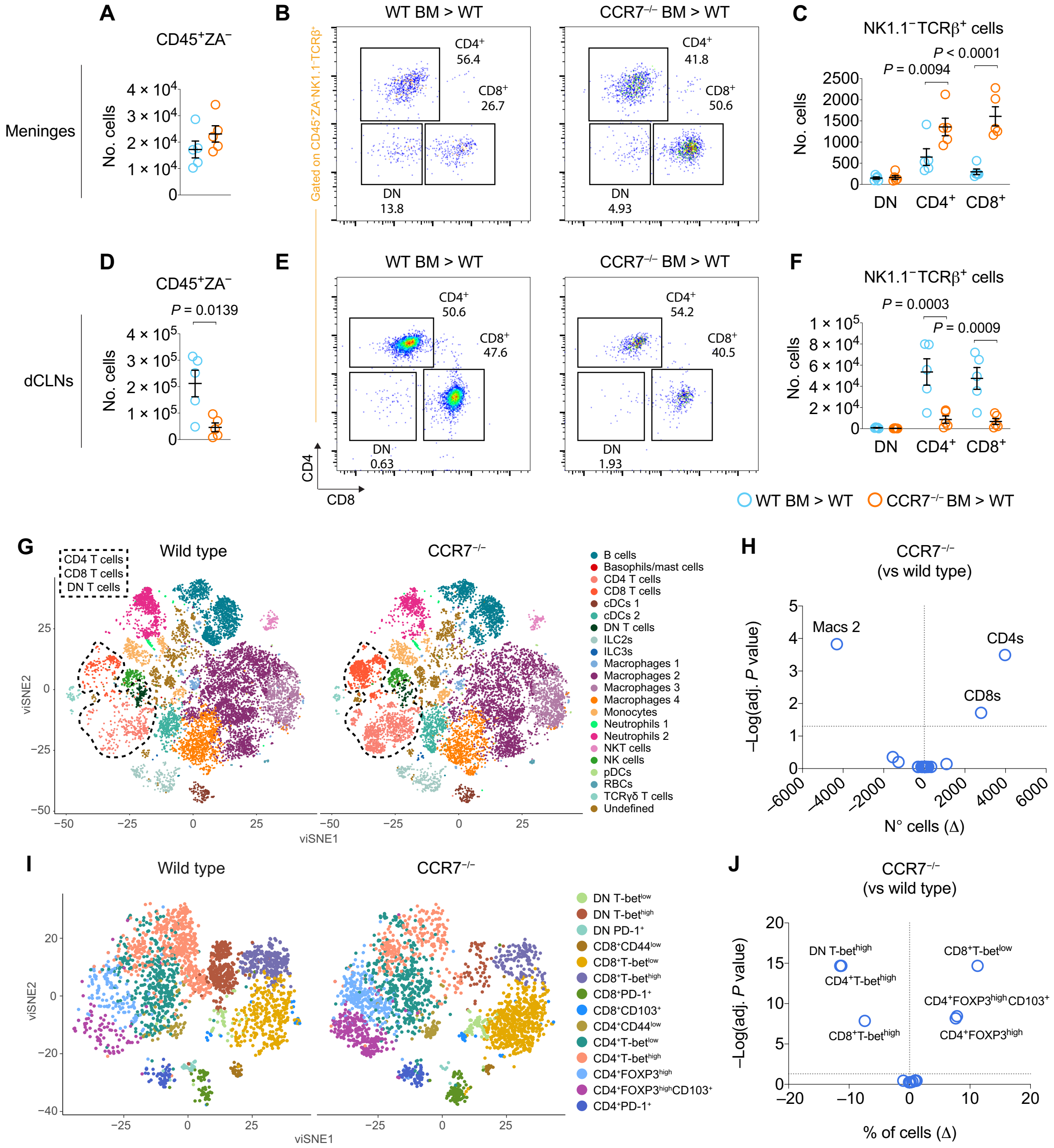

Fig. 2. CCR7 deficiency in hematopoietic cells mimics the aging-related dysregulated meningeal T cell response. (**A** to **F**) Bone marrow (BM) from 2-month-old WT or CCR7-deficient (CCR7$^{-/-}$) mice was transferred into irradiated (head-covered) WT recipients (6 weeks old). Immune response and behavior were assessed 10 weeks later. Quantification of CD45$^+$ZA$^-$ cell number, representative flow cytometry dot plots, and quantification of DN, CD4$^+$, and CD8$^+$ T cell numbers in the (A to C) meninges and (D to F) dCLNs. Data are presented as means ± SEM; $n = 5$ per group; two-tailed unpaired Student's *t* test in (A) and (D); two-way ANOVA with Sidak's multiple comparisons test in (C) and (F). (**G**) *t*-distributed stochastic neighbor embedding–based visualization (viSNE) plots showing unsupervised clustering profile of subpopulations of CD45$^+$ live immune cells. NK cells, natural killer cells; RBCs, red blood cells. (**H**) Volcano plot with change in frequency (in percentage) of subpopulations of meningeal leukocytes in CCR7$^{-/-}$ mice (relative to WT, $n = 5$ per group). Individual data points represent the mean for each leukocyte population; multiple two-tailed unpaired Student's *t* tests with two-stage step-up method of Benjamini, Krieger, and Yekutieli and false discovery rate (FDR) (Q) = 0.05. (**I**) viSNE plots showing clustering of subpopulations of meningeal CD4, CD8, and DN T cells. (**J**) Volcano plot with change in frequency (%) of subpopulations of meningeal CD4, CD8, and DN T cells in CCR7$^{-/-}$ mice (relative to WT, $n = 5$ per group). Individual data points represent the mean for each T cell population; multiple two-tailed unpaired Student's *t* tests with two-stage step-up method of Benjamini, Krieger, and Yekutieli and FDR (Q) = 0.05. cDCs1, conventional dendritic cells 1; ILC2s, type 2 innate lymphoid cells; NKT, natural killer T; pDCs, plasmacytoid dendritic cells.

the observed deficit in glymphatic function, we evaluated AQP4 in the brains of CCR7$^{-/-}$ mice. We found that brain vascular coverage by AQP4 was significantly reduced in both germline CCR7$^{-/-}$ mice (fig. S6, K to M) and adult WT mice that had received CCR7$^{-/-}$ bone marrow (fig. S6, N to P). Further investigation will be needed to determine whether the heightened T$_{\text{reg}}$ response observed in the meninges and dCLNs of these CCR7$^{-/-}$ mice is accountable for the observed reductions in brain AQP4 coverage and CSF influx

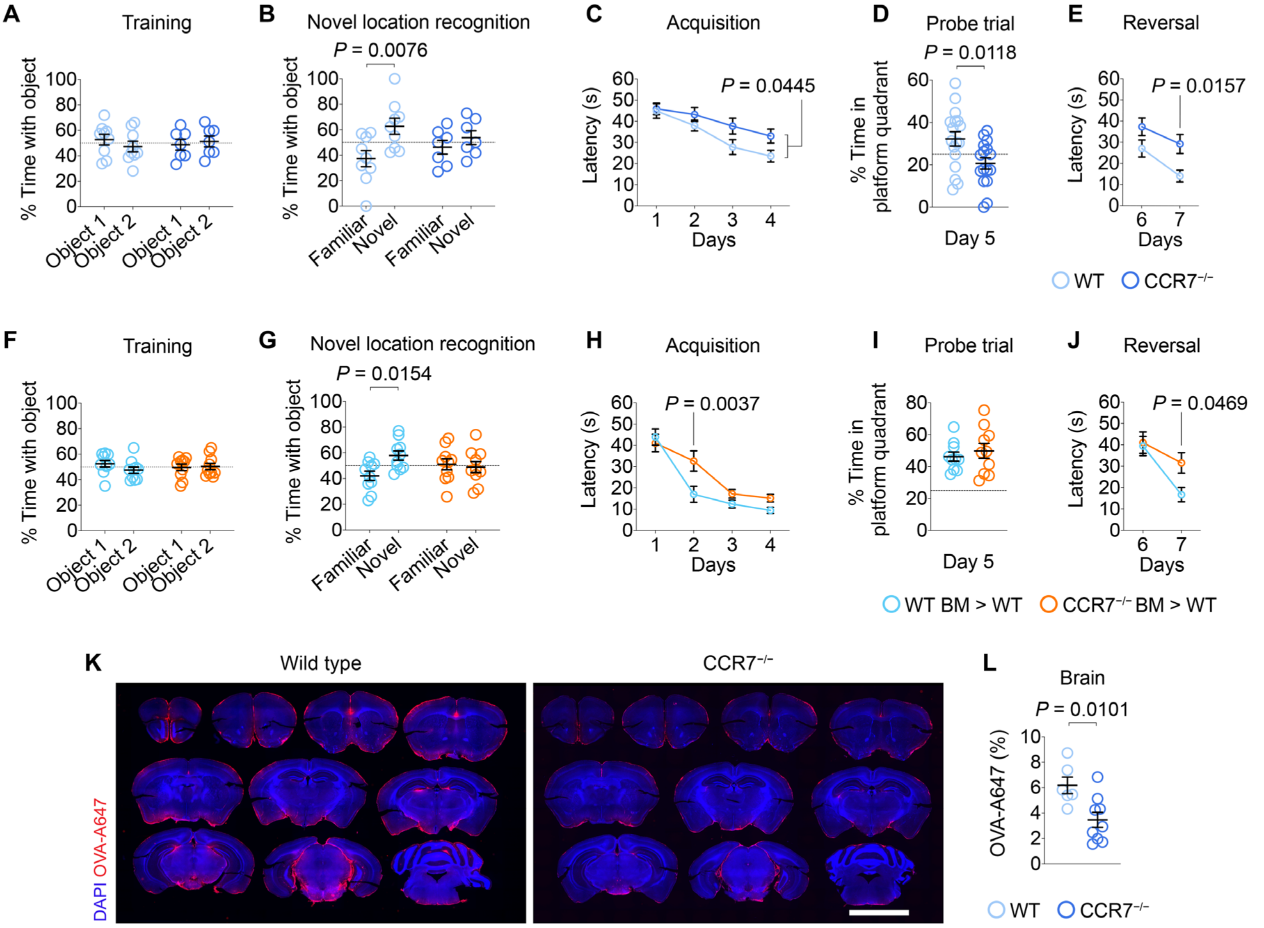

Fig. 3. CCR7$^{-/-}$ mice show cognitive deficits and decreased brain glymphatic function. (**A** and **B**) Graphs showing the percentage of time exploring the objects in the (A) training session or (B) novel location recognition test. Data are presented as means ± SEM; *n* = 9 in WT and *n* = 7 in CCR7$^{-/-}$, littermates with 5 to 7 months of age; two-way ANOVA with Sidak's multiple comparisons test. (**C** to **E**) MWM (C) latency to platform in acquisition, (D) percentage of time in the target quadrant in probe, and (E) latency to platform in reversal. Data are presented as means ± SEM; *n* = 17 in WT and *n* = 16 in CCR7$^{-/-}$, littermates with 5 to 7 months of age; repeated-measures two-way ANOVA with Sidak's multiple comparisons test in (C) and (E); two-tailed unpaired Student's *t* test in (D); data were pooled from two independent experiments. (**F** and **G**) Graphs showing the percentage of time exploring the objects in the (F) training session or (G) novel location recognition test. Data are presented as means ± SEM; *n* = 10 per group, mice with 4 months of age; two-way ANOVA with Sidak's multiple comparisons test. (**H** to **J**) MWM (H) latency to platform in acquisition, (I) percentage of time in the target quadrant in probe, and (J) latency to platform in reversal. Data are presented as means ± SEM; *n* = 10 per group, mice with 4 months of age; repeated-measures two-way ANOVA with Sidak's multiple comparisons test in (H) and (J); two-tailed unpaired Student's *t* test in (I). (**K**) Representative brain sections depicting fluorescent ovalbumin (OVA) in red (OVA-A647) and cell nuclei in blue. Scale bar, 5 mm. (**L**) Quantification of OVA-A647 in brain sections. Data are presented as means ± SEM; *n* = 6 in WT and *n* = 9 in CCR7$^{-/-}$, littermates with 5 to 7 months of age; two-tailed unpaired Student's *t* test; representative of two independent experiments.

through the glymphatic system. Nevertheless, our data indicate that impaired spatial memory and glymphatic function are a consequence of hematopoietic CCR7 deficiency, even when drainage of CSF solutes by the meningeal lymphatic vasculature is intact.

AD transgenic mice show accelerated brain Aβ deposition and cognitive decline in the absence of CCR7

To examine the role of CCR7 in AD-like pathophysiology, we used the 5xFAD transgenic mouse model of familial AD. We found that middle-aged 5xFAD mice (12 to 14 months old; heterozygous for CCR7^{GFP}), when compared to their younger counterparts (3 months old; heterozygous for CCR7^{GFP}), showed a significant decrease in CCR7-expressing T cells in the meninges and dCLNs (Fig. 4, A and B), but not in the blood or liver (fig. S7, A and B). To investigate whether a decrease in CCR7 would affect Aβ clearance from the brain, we generated 5xFAD mice lacking CCR7 expression (5xFAD::CCR7$^{-/-}$). In 5-month-old 5xFAD::CCR7$^{-/-}$ mice, analysis of meningeal immunity by CyTOF revealed an increased number of different leukocyte subpopulations (macrophages, neutrophils, B cells, and T cells) (fig. S7, C and D). Similar to nontransgenic CCR7$^{-/-}$ mice (Fig. 2, I and J), the 5xFAD::CCR7$^{-/-}$ mice demonstrated an increased frequency of CD4^{+}FOXP3^{+} T$_{\text{regs}}$ in the meninges, at the expense of T-bet$^{\text{high}}$ T cells (Fig. 4, C and D).

The heightened T$_{\text{reg}}$ response in 5xFAD mice lacking CCR7 could be especially important in light of prior evidence showing that either the presence of T$_{\text{regs}}$ at the blood-CSF barrier or increased expression of the anti-inflammatory cytokine interleukin-10 plays a detrimental role in the progression of AD-like brain pathology and cognitive decline (*8*, *40*, *41*). The abnormal meningeal immune response observed here in 5xFAD::CCR7$^{-/-}$ mice was accompanied

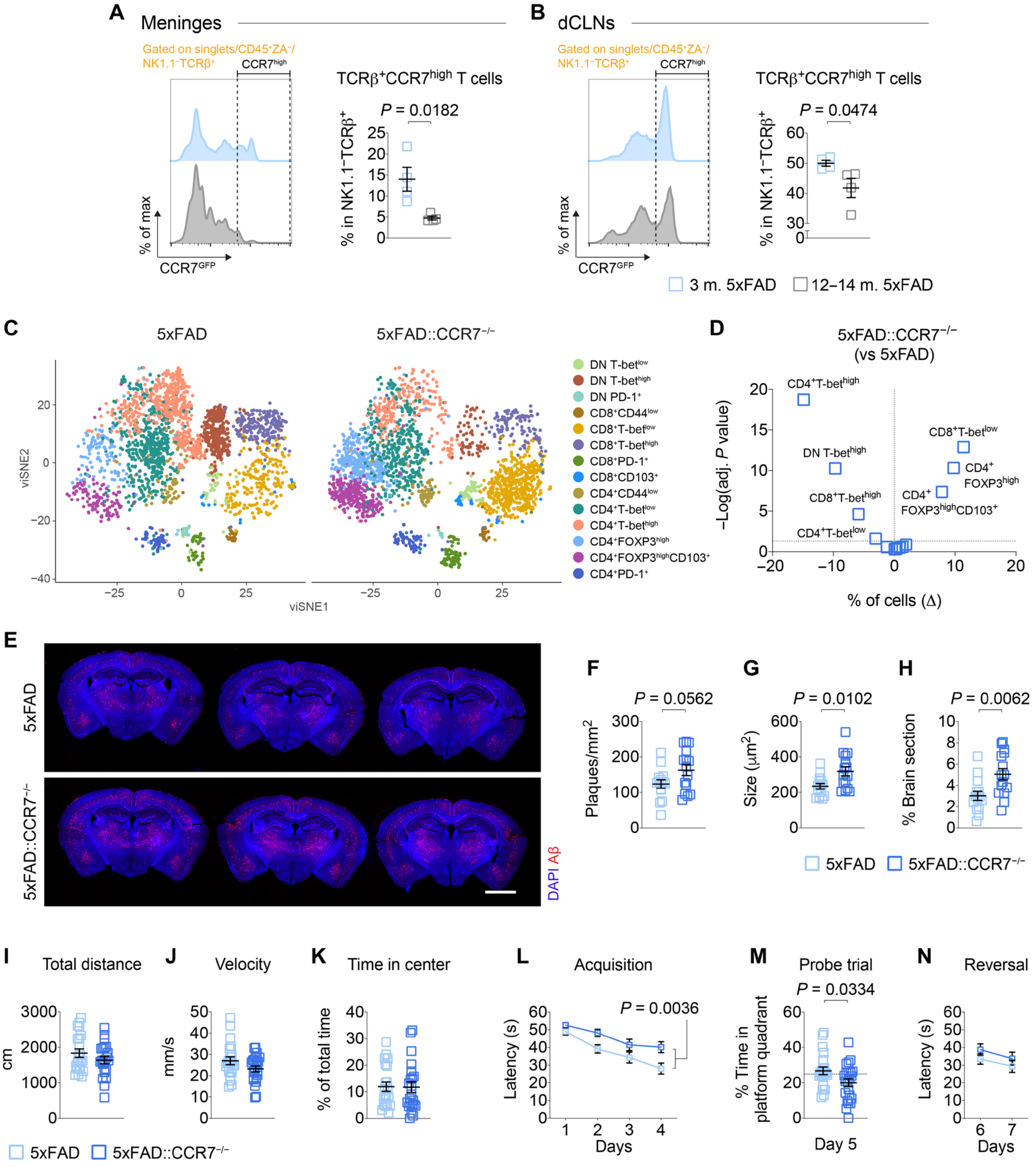

Fig. 4. CCR7 deficiency heightens the meningeal T_{reg} response, aggravates brain Aβ plaque burden, and precipitates spatial memory deficits in 5xFAD mice. (**A** and **B**) Representative histograms and quantification of $CCR7^{high}$ cell frequency in the (A) meninges or (B) dCLNs. Data are presented as means ± SEM; $n = 4$ per group; two-tailed unpaired Student's *t* test. (**C**) viSNE plots showing clustering of subpopulations of meningeal CD4, CD8, and DN T cells. (**D**) Volcano plot with change in frequency (in percentage) of subpopulations of meningeal CD4, CD8, and DN T cells in 5xFAD::$CCR7^{-/-}$ mice (relative to age-matched littermate 5xFAD, $n = 5$ per group). Individual data points represent the mean for each T cell population; multiple two-tailed unpaired Student's *t* tests with two-stage step-up method of Benjamini, Krieger, and Yekutieli and FDR (Q) = 0.05. (**E**) Representative brain sections showing Aβ in red and cell nuclei in blue. Scale bar, 2 mm. (**F** to **H**) Graphs showing quantification of Aβ (F) plaques per square millimeter, (G) plaque average size (in square micrometers), (H) and coverage of Aβ (percentage of brain section). Data are presented as means ± SEM; $n = 14$ in 5xFAD and $n = 15$ in 5xFAD::$CCR7^{-/-}$; two-tailed unpaired Student's *t* tests in (F) to (H); data were pooled from two independent experiments. (**I** to **K**) Graphs showing the open-field (I) total distance (in centimeters), (J) velocity (in millimeters per second), and (K) percentage of time in center. Data are presented as means ± SEM; $n = 21$ in 5xFAD and $n = 22$ in 5xFAD::$CCR7^{-/-}$, littermates with 4 to 5 months of age; two-tailed unpaired Student's *t* test in (I to K); data were pooled from two independent experiments. (**L** to **N**) MWM (L) latency to platform in acquisition trials, (M) percentage of time in the target quadrant in probe trial, and (N) latency to platform in reversal trials. Data are presented as means ± SEM; $n = 21$ in 5xFAD and $n = 22$ in 5xFAD::$CCR7^{-/-}$, littermates with 4 to 5 months of age; repeated-measures two-way ANOVA with Sidak's multiple comparisons test in (L) and (N); two-tailed unpaired Student's *t* test in (M); data were pooled from two independent experiments.

by an increase in brain Aβ plaque burden (Fig. 4, E to H), but not in the number of ionized calcium binding adaptor molecule 1 (IBA1$^+$) myeloid cells clustering around the plaques (fig. S7, E and F). Moreover, as indicated by the significantly lower density of peri-plaque IBA1$^+$ cells in the 5xFAD::CCR7$^{-/-}$ group, the increased Aβ deposition in the brain cortex of these mice was not followed by an increase in plaque containment by IBA1$^+$ cells (fig. S7G). Since CD11b$^+$CD45^{int} myeloid cells from the 5xFAD brain do not express CCR7 (fig. S7H), this apparent inability of parenchymal myeloid cells to contain the larger Aβ plaques may be attributable to a nonautonomous mechanism, for example, an enhanced immunosuppressive activity by meningeal T$_{regs}$ in 5xFAD::CCR7$^{-/-}$ mice. Increased meningeal deposition of Aβ, an important pathological feature of AD, was shown to be aggravated upon pharmacological ablation of meningeal lymphatic vessels (*17*, *28*). However, mice lacking CCR7 did not show increased meningeal amyloid angiopathy (fig. S7, I and J), which is probably attributable to their intact and functional meningeal lymphatic system (fig. S6, G to J). These observations suggest that the altered immunity incurred by CCR7 deficiency contributes to brain Aβ deposition, but not to meningeal amyloid angiopathy.

Besides brain and meningeal Aβ pathology, another prominent clinical feature of AD is the emergence of behavioral deficits, such as accelerated cognitive decline (*3*). To determine whether decreased CCR7 expression could precipitate behavioral deficits in AD, we assessed the performance of adult littermates 5xFAD and 5xFAD::CCR7$^{-/-}$ mice, all 4 to 5 months old, in the open-field and in MWM tests (Fig. 4, I to N). Loss of CCR7 expression in 5xFAD mice did not affect exploratory or anxiety-like behaviors (Fig. 4, I to K), but it did worsen spatial learning and memory (Fig. 4, L to N).

CCR7 deficiency disrupts brain vascular and microglial activation in 5xFAD mice

To deepen our understanding of the consequences of decreased CCR7 expression for the neuroinflammatory response in AD, we analyzed the transcriptional alterations in blood endothelial cells (BECs) and myeloid cells isolated from the brains of 5-month-old 5xFAD and 5xFAD::CCR7$^{-/-}$ littermates by single-cell RNA sequencing (RNA-seq; Fig. 5A). Using this approach, we were able to identify five distinct brain cell clusters, each expressing specific canonical markers (fig. S8A): namely, microglia, border-associated macrophages (BAMs), arterial BECs, capillary BECs, and venous BECs (Fig. 5B). Although no genotype-associated segregation was apparent within the clusters of BECs or BAMs, we observed clear differences between microglia isolated from the 5xFAD and from the 5xFAD::CCR7$^{-/-}$ mice (Fig. 5C). Analysis of differentially expressed genes in the mice lacking CCR7 revealed an interesting dichotomy, with brain BECs (with the exception of venous BECs) showing a higher number of down-regulated genes and brain myeloid cells showing a higher number of up-regulated genes (Fig. 5, D to F, and fig. S8, B and C). Lysosome-related cathepsin genes, including *Ctsb*, *Ctsd*, *Ctsl*, *Ctss*, and *Ctsz*, were up-regulated in both vascular and myeloid cells (Fig. 5, D to F, and fig. S8, B and C). The *Cst3* gene, which encodes for the cystatin C protein, was also significantly up-regulated in brain BECs from the 5xFAD::CCR7$^{-/-}$ mice (Fig. 5, D and E, and fig. S8B), suggesting a potential vascular lysosomal dysfunction accompanying the increased cerebral Aβ burden in these mice (*42*, *43*). Up-regulated genes in BECs were implicated in pathways termed "antigen processing and presentation of peptide antigen," "myeloid leukocyte migration," and "positive regulation of immune effector process" (Fig. 5, G and H, and fig. S8D, respectively). Up-regulated genes in BAMs were implicated in similar pathways (fig. S8E), possibly owing to their proximity and potential interactions. On the other hand, gene ontology terms obtained from genes that were down-regulated in arterial and capillary BECs from 5xFAD::CCR7$^{-/-}$ mice included "regulation of vasculature development," "regulation of angiogenesis," "endothelial cell migration," and "actin filament organization" (Fig. 5, G and H).

Apoe, *Axl*, *Fth1*, *Lpl*, *Lyz2*, and *Trem2*, genes previously implicated in the development of brain amyloidosis in AD transgenic mouse models (*11*, *12*, *44*), were found among the 718 genes that were overexpressed in microglia from 5xFAD::CCR7$^{-/-}$ mice (Fig. 5F). The up-regulated microglial genes were involved in processes such as "cytoplasmic translation," "adenosine 5′-triphosphate (ATP) metabolic process," "defense response to virus," and "negative regulation of immune system process" (Fig. 5I). Conversely, gene ontology terms relating to down-regulated genes in microglia from 5xFAD::CCR7$^{-/-}$ mice included "anatomical structure homeostasis," "dendrite development," and "selective autophagy" (Fig. 5I).

Old mice treated with anti-CD25 antibodies show improved cognition and lower T$_{reg}$ frequencies

In seeking to understand the therapeutic effects of reshaping the immune response in old mice, we assessed the performance of 25-month-old mice in different behavioral tests in response to a treatment regimen with anti-CD25 antibodies or with control [immunoglobulin G (IgG)] antibodies (Fig. 6A). Old mice injected with IgG or anti-CD25 antibodies performed similarly in the open-field test and in the training trial of the novel location-recognition test (fig. S9, A to D). However, mice that had received anti-CD25 antibodies showed improved spatial learning and memory, as indicated mainly by their better performance in the MWM (significantly lower latency to platform; Fig. 6, B to D) and in the novel location-recognition testing trial (higher percentage of time in the novel location; Fig. 6E). The improved cognitive function achieved by treating the old mice with anti-CD25 antibodies was accompanied by a significant reduction in CD4$^+$FOXP3$^+$ T$_{regs}$ in the meninges (Fig. 6, F to I) and dCLNs (Fig. 6, J to M), but not in the blood (fig. S9, E to G) or liver (Fig. 6, H to J).

DISCUSSION

Together, our results provide evidence highlighting the adverse effects of an aging-related decrease in CCR7 expression on meningeal immunity and brain immune surveillance, glymphatic function, Aβ deposition, and cognition (fig. S10). Loss of CCR7 expression in adult mice resulted in an enhanced meningeal T$_{reg}$ response, a diminished meningeal effector T cell response (with reduced IFN-γ–producing CD4 T cells), and cognitive impairment, suggesting that the decreased expression of CCR7 in aging might underlie the heightened meningeal T$_{reg}$ response and contributes to the aging-associated cognitive decline. Compared with healthy controls, patients with mild cognitive impairment or AD have increased peripheral CD4$^+$CD25^{high}FOXP3$^+$ T$_{regs}$ (*45*). Notably, mitigation of the T$_{reg}$ response in mouse models of AD was shown to have beneficial effects on Aβ clearance, neuroinflammation, and cognition (*8*).

Our experimental data also support the notion that the improved cognitive function in old mice achieved by treatment with anti-CD25 antibodies is closely associated with a reduced T$_{reg}$ response

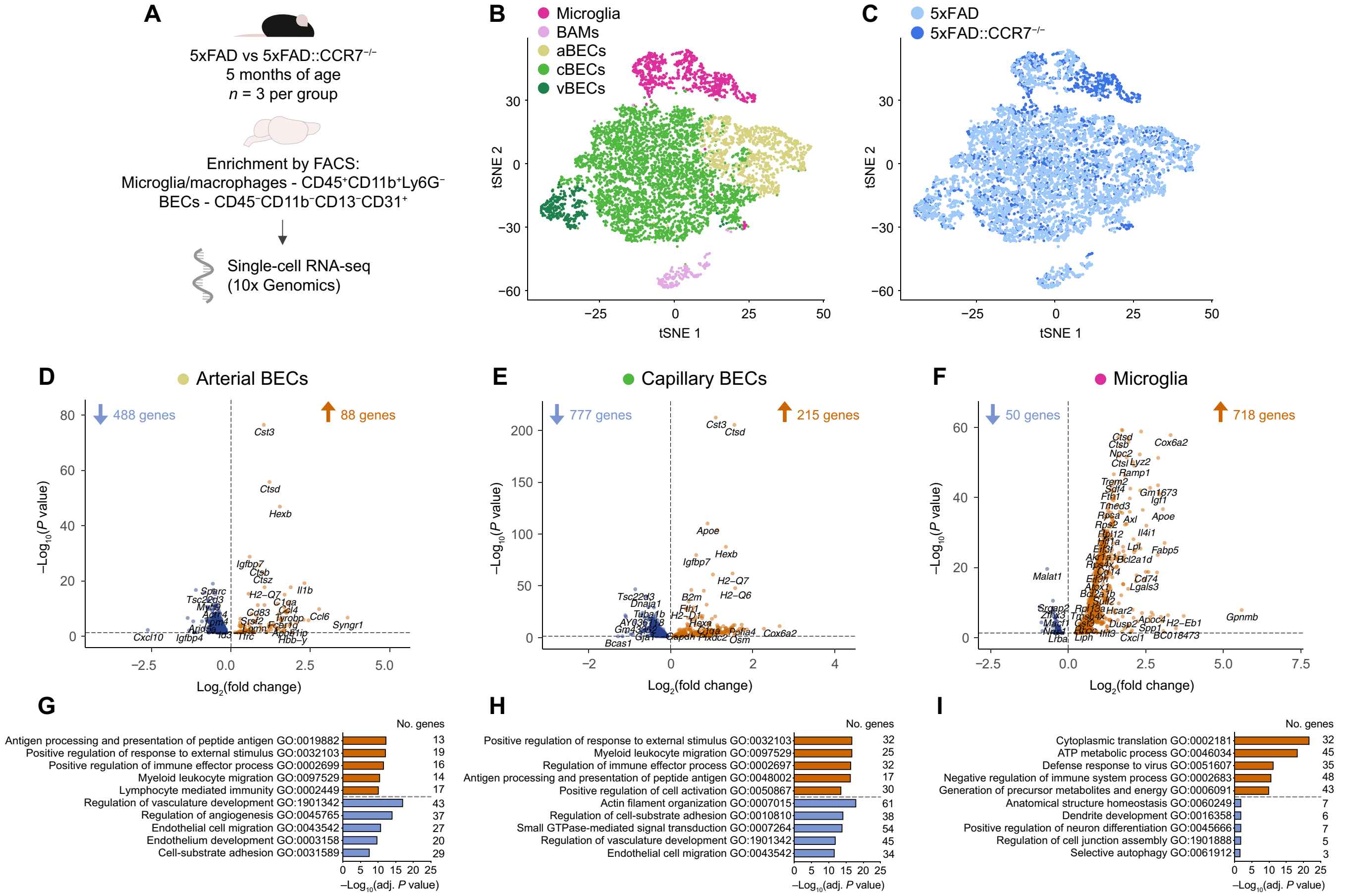

Fig. 5. CCR7 deficiency affects the transcriptional profile of brain BECs and microglia in 5xFAD mice. (**A**) Enrichment for brain myeloid cells (microglia/macrophages) and BECs (brain cell suspensions were pooled from three mice per group at 5 months) was achieved by fluorescence-activated cell sorting (FACS), and transcriptomes were analyzed by single-cell RNA-seq. (**B**) Representation of the t-stochastic neighbor embedding (tSNE) plot highlighting the different clusters of sequenced brain cells, including microglia, BAMs, arterial BECs (aBECs), capillary BECs (cBECs), and venous BECs (vBECs). (**C**) Representation of the tSNE plot highlighting the sequenced brain cells from each group. (**D** to **F**) Volcano plots showing the significantly down-regulated (in blue) and up-regulated (in dark orange) genes between (D) arterial BECs, (E) capillary BECs, and (F) microglia from the 5xFAD::CCR7$^{-/-}$ mice and control 5xFAD mice. (**G** to **I**) Ten gene ontology (GO) terms (selected from the top 20 terms with lowest adjusted *P* value) obtained after analyzing significantly up-regulated (in dark orange) and down-regulated (in blue) genes in (G) arterial BECs, (H) capillary BECs, and (I) microglia. GTPase, guanosine triphosphatase. Data resulted from the analysis of a total of 8567 cells, including 1442 arterial BECs, 5181 capillary BECs, 453 venous BECs, 1176 microglia, and 315 BAMs; differentially expressed genes plotted in (D) to (F) were determined using an *F* test with adjusted degrees of freedom based on weights calculated per gene with a zero-inflation model and Benjamini-Hochberg corrected *P* values; gene ontology analyses in (G) to (I) used overrepresentation test, and terms were selected on the basis of Benjamini-Hochberg corrected *P* values.

in the meninges and dCLNs. However, we have not determined whether there is a concomitant increase in meningeal IFN-γ–producing CD4 T cells that could be contributing to the improved behavioral phenotype (*8*, *22*, *46*). Future studies should be aimed at understanding the functional mechanisms linking the decreased T cell expression of CCR7 with an enhanced meningeal T_{reg} response and whether immunosuppressive meningeal T_{regs} contribute directly to the reduction in T-bet^{high} IFN-γ–producing CD4 T cells in the meninges, impaired brain cleansing, and cognitive decay in AD. The changes in meningeal effector T cells and T_{regs} cells observed in 5xFAD mice lacking CCR7 were accompanied by altered numbers of meningeal macrophages, neutrophils, and B cells. Unexpectedly, the numbers of meningeal macrophages were reduced in nontransgenic adult CCR7$^{-/-}$ mice but increased in 5xFAD::CCR7$^{-/-}$ mice. The latter might be attributable, at least in part, to the heightened degree of amyloidosis, neuroinflammation, and BAM activation observed in 5xFAD::CCR7$^{-/-}$ mice. Given the important role of protective monocytes and macrophages in modulating brain pathology and behavior in AD models (*8*, *10*, *47*), it will be worth investigating whether these observed changes in meningeal macrophages are contributing to the worsened cognitive performance and increased Aβ deposition in the brains of CCR7$^{-/-}$ mice. The same applies to the altered response by meningeal neutrophils and B cells observed in 5xFAD::CCR7$^{-/-}$ mice, which might also be contributing to the exacerbated disease phenotype (*31*, *48*). It will also be of interest to find out whether the described changes in meningeal immunity with aging and with loss of CCR7 expression can be attributed to an altered communication between the immune environments of the meninges and the skull bone marrow (*49*, *50*).

Recent work has indicated that peripheral T cells infiltrate the brain to regulate microglial maturation and phenotype (*51*). It is possible that dysregulated meningeal immunity due to decreased

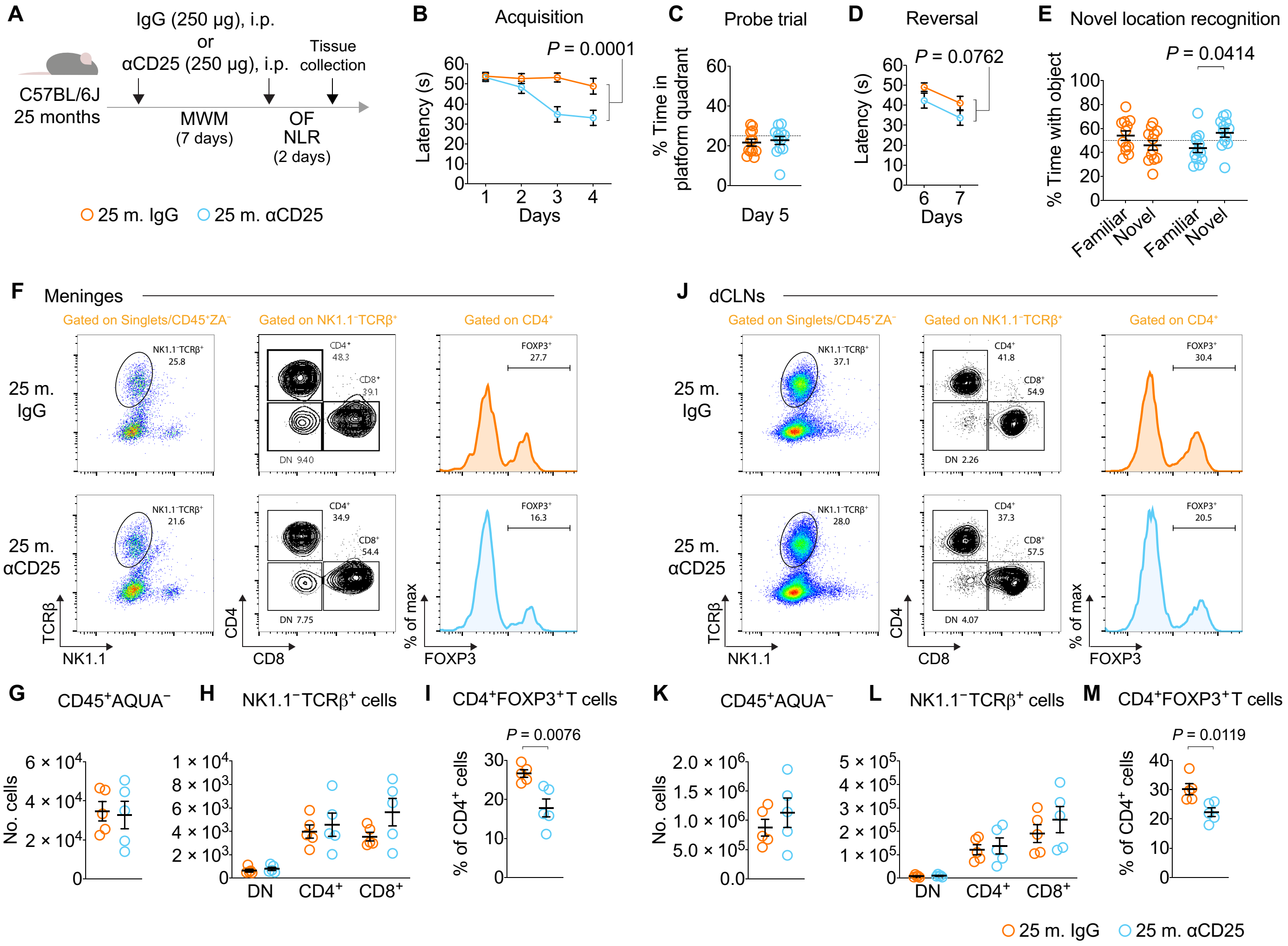

Fig. 6. Treating old mice with anti-CD25 antibodies enhances cognitive function and normalizes FOXP3$^+$ T$_{reg}$ frequencies in the meninges and dCLNs. (**A**) Diagram showing doses and time points of intraperitoneal (i.p.) injections of control IgG1 or anti-CD25 (αCD25) antibodies into mice at 25 months. OF, open field; NLR, novel location recognition. (**B** to **D**) Graphs showing the MWM (B) latency to platform in acquisition, (C) percentage of time spent in the target quadrant in probe, and (D) latency to platform in reversal. Data are presented as means ± SEM; *n* = 12 per group; repeated-measures two-way ANOVA with Sidak's multiple comparisons test in (B) and (D); two-tailed unpaired Student's *t* test in (C); representative of two independent experiments. (**E**) Graph showing the percentage of time exploring the objects during the novel location recognition test. Data are presented as means ± SEM; *n* = 12 per group; two-way ANOVA with Sidak's multiple comparisons test. (**F** to **I**) Panels showing (F) representative flow cytometry dot and contour plots used to calculate the numbers of (G) total CD45$^+$ZA$^-$ cells, (H) DN, CD4$^+$, and CD8$^+$ T cells and frequencies of (I) CD4$^+$FOXP3$^+$ T cells (percentage of CD4$^+$ T cells) in the meninges. (**J** to **M**) Panels showing (J) representative flow cytometry dot and contour plots used to calculate the numbers of (K) total CD45$^+$ZA$^-$ cells, (L) DN, CD4$^+$ and CD8$^+$ T cells, and frequencies of (M) CD4$^+$FOXP3$^+$ T cells (percentage of CD4$^+$ T cells) in the dCLNs. Data are presented as means ± SEM; *n* = 5 per group; two-tailed unpaired Student's *t* test in (G), (I), (K), and (M); two-way ANOVA with Sidak's multiple comparisons test in (H) and (L); representative of two independent experiments.

CCR7 expression alters astrocytic and microglial function in the aging brain, thereby affecting glymphatics and brain Aβ buildup. Our single-cell transcriptional profiling of microglia from AD-transgenic mice lacking CCR7 indicated a metabolic reprogramming, an aberrant activation, and a deficient support of neuronal function, all concomitant with their inability to restrain the Aβ-plaque buildup in the brain. However, more in-depth studies are needed to fully disclose the functional connections between the age-dependent alteration of meningeal immune cell egress, the enhanced meningeal T$_{reg}$ response, and the impact of the latter on glial fitness in the AD brain (*11*, *52*). In the present study, loss of CCR7 also resulted in marked changes in gene expression in brain BECs, which, together with the reduced levels of AQP4, might be contributing to the reduction in glymphatic function. It is still unclear, however, whether the induction of gene pathways participating in vascular activation and leukocyte extravasation and the down-regulation of genes regulating vascular organization, repair, and development are direct consequences of the exacerbated T$_{reg}$ and deficient effector T cell responses observed in the meninges of CCR7$^{-/-}$ mice. Possible effects of decreased CCR7 expression on other pathophysiological aspects of AD, such as the formation of intracellular tau tangles or neuronal death, should also be further investigated. Boosting of CCR7-mediated immune cell egress might prove to be an efficient strategy for counteracting cognitive decline in normal aging and in AD.

MATERIALS AND METHODS

Experimental design

The objective of this study was to assess the effect of aging on CCR7 expression at the brain and meninges and to understand whether a deficit in CCR7 expression could affect the meningeal immunity, brain cleansing and function, and the degree of Aβ pathology and cognitive decline in a transgenic mouse model of familial AD. We used mouse tissue single-cell suspensions, namely from CCR7^{GFP} reporter mice, and flow cytometry to show that aging induces alterations in the conventional and T$_{reg}$ responses in the brain meninges and dCLNs, with a concomitant decrease in T cells expressing CCR7. By performing BMT experiments, we have shown a boost in meningeal T$_{reg}$ response in adult mice that received CCR7$^{-/-}$ bone marrow. CyTOF was used to perform a thorough analysis of the effect of decreased CCR7 expression on the meningeal immune compartment. Behavioral tests were performed to assess brain function in conventional CCR7$^{-/-}$ mice or in mice upon CCR7$^{-/-}$ BMT. Injection of fluorescent peptide tracers into the CSF and collection, immunofluorescent staining, and analysis of brain, dCLNs, and meningeal whole mounts was used to assess brain glymphatic and meningeal lymphatic function in CCR7$^{-/-}$ mice. Assessment of meningeal immunity (by CyTOF), brain Aβ pathology, and behavior was performed in 5xFAD::CCR7$^{-/-}$ mice and respective 5xFAD littermate controls. The effects of CCR7 deficiency on the transcriptional profile of brain BECs and myeloid cells from 5xFAD mice were analyzed by single-cell RNA-seq. Old mice treated with anti-CD25 antibodies showed a lessened T$_{reg}$ response. Flow cytometric analysis of the T cell response in different tissues, as well as the performance in different behavior tests, was assessed after injections of anti-CD25 or control isotype antibodies. Together, the findings presented here connect the decreased CCR7-dependent meningeal T cell egress and altered T$_{reg}$ response, which is observed during aging, with changes in brain glymphatic function, brain vascular and microglial response, Aβ burden, and cognition.

Mouse strains and housing

Adult (2 to 4 months of age) male C57BL/6J WT mice were purchased from the Jackson laboratory (JAX stock #000664, Bar Harbor, Maine, USA). Aged (20 to 25 months old) WT mice were provided by the National Institutes of Health/National Institute on Aging (Bethesda, MD, USA). All mice were maintained in the animal facility for habituation for at least 1 week before the start of the experiment. Male hemizygous C57BL/6.Cg-Tg(*APPSwFlLon, PSEN1*M146L*L286V*)6799Vas/Mmjax (5xFAD, JAX stock #008730), heterozygous C57BL/6-*Ccr7*$^{tm1.1Dnc}$/J (CCR7^{GFP}, JAX stock #027913), and C57BL/6.129P2(C)-*Ccr7*^{tm1Rfor}/J (CCR7$^{-/-}$, JAX stock #006621) were purchased from the Jackson Laboratory and bred in-house on a C57BL/6J background. All experiments were performed using mice heterozygous for the CCR7^{GFP} reporter gene. In-house crossings were performed to obtain mice heterozygous for CCR7^{GFP} or deficient for CCR7 (CCR7$^{-/-}$) on a nontransgenic or 5xFAD background (hemizygous for the transgene). Aged-matched littermate controls were used in experiments involving CCR7$^{-/-}$ (control group designated as WT) and 5xFAD::CCR7$^{-/-}$ mice (control group designated as 5xFAD). Mice with the appropriate genotypes were used at different ages, as indicated in figure schemes, legends, or in the main text throughout the manuscript. Only male mice were used in all the experiments. Mice of all strains were housed in an environment with controlled temperature and humidity and on a 12-hour light/dark cycle (lights on at 7:00 a.m.). All mice were fed with regular rodent's chow and sterilized tap water ad libitum. All experiments were approved by the Institutional Animal Care and Use Committee of the University of Virginia and Washington University in St. Louis.

Irradiation and BMT

Age-matched mice were exposed to a lethal dose of γ radiation (10 Gy) throughout the body, except for the head that was protected with a lead shield. Approximately 4 hours after irradiation, mice were intravenously injected with 1×10^7 bone marrow cells. Mice were monitored daily for the first 4 days and given water supplemented with trimethoprim-sulfamethoxazole for 2 weeks following irradiation.

Intraperitoneal injections with antibodies

Old mice (25 months old) received intraperitoneal injections of rat IgG1 (250 μg total; clone HRPN, BE0088, Bio X Cell) or anti-CD25 (250 μg total; clone PC-61.5.3, BE0012, Bio X Cell) antibodies, in InVivoPure pH 7.0 dilution buffer (Bio X Cell, IP0070). Mice were injected with the same amounts of antibodies 1 week later, after performing the MWM and before performing the open-field and novel location recognition tests.

Open-field test

Mice were habituated to the behavior room, including the background white noise, for at least 30 min before starting the test. Individual mice were then placed into the open-field arena (made of opaque white plastic material, 35 cm by 35 cm) by a blinded experimenter and allowed to explore it for 15 min. Total distance (in centimeters), velocity (in millimeters per second), and percentage of time spent in the center (22 cm by 22 cm area) were quantified using video tracking software (TopScan, CleverSys Inc.) and analyzed in Microsoft Excel and Prism 8.3.4 (GraphPad Software Inc.).

Novel location recognition test

Mice were habituated to the behavior room and background white noise for at least 30 min. The experimental apparatus used in this study was the same square box made of opaque white plastic (35 cm by 35 cm) used in the open-field test, which made habituation to the apparatus unnecessary. Briefly, two different plastic objects (with different colors and shapes) were then positioned in a defined spatial orientation, namely on each corner of the arena and 5 cm away from each adjacent arena wall. Mice were then placed in the arena (by a blinded experimenter), facing the wall farther away from the objects, and allowed to explore the arena and objects for 10 min (training). Twenty-four hours later, mice were placed in the same box but with one of the objects switched to a novel location, namely in a new quadrant obliquely to the object in the familiar location. The time spent exploring the objects in the familiar and novel locations was also measured for 10 min (novel location recognition). Exploration of an object was assumed when the mouse approached an object and touched it with its vibrissae, snout, or forepaws and was measured using a video tracking software (TopScan, CleverSys Inc.). The object location preference (percentage of time with object) was calculated in Excel as the exploration time of each object (in the familiar or in the novel locations) divided by the total object exploration time.

MWM test

The MWM test was performed as described before (*28*), with minor modifications. Mice were habituated to the behavior room, including the background white noise, for at least 30 min before starting the test. The MWM test consisted of 4 days of acquisition, 1 day of probe trial, and 2 days of reversal. In the acquisition, mice performed four trials per day, for four consecutive days, to find a hidden 10-cm-diameter platform located 1 cm below the water surface in a pool of 1 m in diameter. Tap water was made opaque with nontoxic white paint (Prang ready-to-use washable tempera paint), and the water temperature was kept at 25° ± 1°C by addition of warm water. A dim light source was placed within the testing room, and only distal visual cues were available above each quadrant of the swimming pool to aid in the spatial navigation and location of the submerged platform. The latency to platform, i.e., the time required by the mouse to find and climb onto the platform, was recorded for up to 60 s. Each mouse was allowed to remain on the platform for ~15 s and was then moved from the maze to its home cage. If the mouse did not find the platform within 60 s, then it was manually placed on the platform and returned to its home cage after ~15 s. The intertrial interval for each mouse was of at least 5 min. On day 5, the platform was removed from the pool, and each mouse was tested in a probe trial for 60 s. On days 1 and 2 of the reversal, without changing the position of the visual cues, the platform was placed in the quadrant opposite to the original acquisition quadrant, and the mouse was retrained for four trials per day. All MWM testing was performed between 10:00 a.m. and 6:00 p.m., during the lights-on phase, by a blinded experimenter. During the acquisition, probe, and reversal, data were recorded using the EthoVision automated tracking system (Noldus Information Technology). The mean latency (in seconds) of the four trials for each day of test and the percentage of time in the platform quadrant during the probe trial were calculated in Excel and analyzed in Prism 8.3.4.

Intracisterna magna injections

Mice were anesthetized by intraperitoneal injection of a mixed solution of ketamine (100 mg/kg) and xylazine (10 mg/kg) in saline. The skin of the neck was shaved and cleaned with iodine and 70% ethanol, and ophthalmic solution placed on the eyes to prevent drying and the mouse's head was secured in a stereotaxic frame. After making a small (4 to 5 mm) skin incision, the muscle layers were retracted, and the atlantooccipital membrane of the cisterna magna was exposed. Using a Hamilton syringe (coupled to a 33-gauge needle), the volume of the desired solution was injected into the CSF-filled cisterna magna compartment at a rate of ~2.5 μl/min. After injecting, the syringe was left in place for at least 2 min to prevent backflow of CSF. The neck skin was then sutured, and the mice were allowed to recover in supine position on a heating pad until fully awake and subcutaneously injected with ketoprofen (2 mg/kg). This method of intracisterna magna injection was used to infuse 5 μl of Alexa Fluor 647–conjugated ovalbumin (OVA) (Thermo Fisher Scientific) in artificial CSF (#597316, Harvard Apparatus U.K.), at a concentration of 1 mg/ml and at a rate of 2.5 μl/min.

Tissue collection and processing

Mice were given a lethal dose of anesthetics by injection of Euthasol [i.p., 10% (v/v) in saline] and transcardially perfused with ice-cold phosphate-buffered saline (PBS) (pH 7.4) with heparin (10 U/ml). dCLNs were dissected and drop-fixed in 4% paraformaldehyde (PFA) for 12 hours at 4°C. After stripping the skin and muscle from the bone, the entire head was collected and drop-fixed in 4% PFA for 24 hours at 4°C. After removal of the mandibles and nasal bone, the top of the skull (skull cap) was removed with fine surgical curved scissors (Fine Science Tools) by cutting clockwise, beginning and ending inferior to the right posttympanic hook, and kept in PBS 0.02% azide at 4°C until further use. Fixed meninges (dura mater and arachnoid) were carefully dissected from the skull caps with Dumont #5 and #7 fine forceps (Fine Science Tools) and kept in PBS 0.02% azide at 4°C until further use. The brains were kept in 4% PFA for an additional 24 hours (at least 48 hours in total). Fixed dCLNs and brains were washed with PBS, cryoprotected with 30% sucrose, and frozen in Tissue-Plus O.C.T. compound (Thermo Fisher Scientific). A cryostat (Leica) was used to slice sections of fixed and frozen dCLNs (30-μm-thick sections) that were collected onto gelatin A–coated slides and kept at −20°C until further use. Fixed and frozen brain sections (50 or 100 μm in thickness) were collected into 12-well plates with PBS 0.02% azide and kept at 4°C until further use.

Immunohistochemistry, imaging, and quantifications

The following steps were generally applied for free-floating brain sections and meningeal whole mounts. For immunofluorescence staining, tissue was rinsed in PBS and incubated with PBS 0.5% Triton X-100 (PBS-T) (Thermo Fisher Scientific) for 30 min, followed by PBS-T containing 0.5% of normal serum (either donkey or chicken; Jackson ImmunoResearch Laboratories Inc.) or 0.5% bovine serum albumin (BSA; Equitech-Bio Inc.) for 30 min at room temperature (RT). This blocking step was followed by incubation with appropriate dilutions of primary antibodies: rat anti–lymphatic vessel endothelial hyaluronan receptor 1 (LYVE)-1–eFluor660 or anti–LYVE-1–Alexa Fluor 488 (clone ALY7, eBioscience; 1:200), rabbit anti-AQP4 (A5971, MilliporeSigma; 1:200), goat anti-IBA1 (ab5076, polyclonal, Abcam; 1:200), and rabbit anti-A$\beta_{1-37/42}$ (8243S, clone D54D2, Cell Signaling Technology; 1:400) in PBS-T containing 0.5% BSA overnight at 4°C. Meningeal whole mounts or brain sections were then washed three times for 10 min at RT in PBS-T, followed by incubation with the appropriate chicken or donkey Alexa Fluor 488– or Alexa Fluor 594–conjugated anti-goat or -rabbit IgG antibodies (Thermo Fisher Scientific; 1:500) for 1 hour at RT in PBS-T. After an incubation for 10 min with 1:5000 4′,6-diamidino-2-phenylindole (DAPI) in PBS, the tissue was washed three times for 5 min with PBS, left to dry at RT (10 to 20 min), and mounted with Shandon Aqua-Mount (Thermo Fisher Scientific) and glass coverslips. A wide-field microscope (DMI6000 B with Adaptive Focus Control, Leica Microsystems) was used to acquire images of Aβ aggregates in brain sections or in meningeal whole mounts. A confocal microscope (FV1200 Laser Scanning Confocal Microscope, Olympus) was used to acquire the rest of the images analyzed in this study. Upon acquisition, images were opened in the Fiji software for quantification. For the assessment of fluorescent OVA-A647 tracer in the brain, 10 representative brain sections were imaged using the wide-field microscope, and the mean area fraction was calculated using Excel. The area fraction of drained fluorescent OVA-A647 tracer was assessed in alternate dCLNs' sections (representing a total of 10 to 15 sections per sample) using Fiji, and the mean was calculated for each sample. For lymphatic vessel diameter (in micrometers), images of the same region of interest (ROI) depicting the transverse sinus were acquired in the confocal microscope, and the mean of 100 individual lymphatic vessel diameter measurements (50 measurements in lymphatic vessels lining each transverse sinus using Fiji) was calculated for each sample. The same images of meningeal whole mounts acquired in the confocal microscope were used to quantify meningeal lymphatic vessel coverage using the Fiji *threshold* and *measure* plugins. Area of coverage by $AQP4^+$ astrocyte endfeet in the brain cortex was achieved with the Fiji *threshold* and *measure* plugins and by calculating the mean value of four representative fields (two images in each cerebral hemisphere) per sample acquired using the confocal microscope. The ROI *manager*, *threshold*, and *measure* plugins were used to measure the coverage by Aβ (as percentage of brain section delineated ROI) in the whole brain section and meninges. The *analyze particles* plugin (size, 4-infinity μm^2; circularity, 0.05 to 1) was used to measure the average size of the plaques (in square micrometers) and calculate plaque density (per square millimeter of brain tissue) in each brain section (plotted values resulted from the average of three representative sections per sample). All measurements were performed by a blinded experimenter, Excel was used to calculate average values in each independent experiment, and the statistical analysis was performed using Prism 8.3.4.

Flow cytometry

Mice were injected with Euthasol or Fatal-Plus [i.p., 10% (v/v) in saline] and were transcardially perfused with ice-cold PBS with heparin. The brains were collected into ice-cold RPMI 1640 (Gibco), and the cortices were dissected after removing hippocampus and remnants of choroid plexus and pia matter. Individual meninges were immediately dissected from the mouse's skull cap in ice-cold RPMI 1640. The tissues were digested for 20 min at 37°C with collagenase VIII (1 mg/ml), collagenase D (1 mg/ml), and deoxyribonuclease I (DNase I) (50 U/ml; all from Sigma-Aldrich) in RPMI 1640. The same volume of RPMI 1640 with 10% fetal bovine serum (FBS; Atlas Biologicals) and 10 mM EDTA (Thermo Fisher Scientific) was added to the digested tissue, which was then filtered through a 70-μm cell strainer (Thermo Fisher Scientific). The cell pellets were washed and resuspended in ice-cold fluorescence-activated cell sorting (FACS) buffer (pH 7.4) (0.1 M PBS, 1 mM EDTA, and 1% BSA) before staining for extracellular markers. Alternatively, for measurement of IFN-γ production, single-cell suspensions were stimulated for 4 hours in Iscove's Modified Dulbecco's Media [supplemented with 1× nonessential amino acids, penicillin (50 U/ml), streptomycin (50 μg/ml), 50 μM β-mercaptoethanol, 1 mM sodium pyruvate, and 10% FBS, all for Gibco] with phorbol 12-myristate 13-acetate/ionomycin (Cell Stimulation Cocktail, eBioscience) and 1× brefeldin A (eBioscience) at 37°C before extracellular staining. For extracellular staining, cells were preincubated for 10 min at 4°C with Fc receptor–blocking solution (anti-CD16/32, clone 93, BioLegend; 1:200 in FACS buffer) and then incubated for 25 min at 4°C with different combinations of the following antibodies (all at 1:200 in FACS buffer): anti–CD4–fluorescein isothiocyanate (FITC; 100406, BioLegend), anti–TCRβ-FITC (109206, BioLegend), anti–CD25–phycoerythrin (PE; 12-0251-83, eBioscience), anti–CD19-PE (553786, BD Biosciences), anti–CD4-PerCP-Cy5.5 (550954, BD Biosciences), anti–CD45-PerCP-Cy5.5 (550994, BD Biosciences), anti–CD11b-PerCP-Cy5.5 (101228, BioLegend) anti–CD103-PerCP-Cy5.5 (121415, BioLegend), anti–TCRβ-PerCP-Cy5.5 (109228, BioLegend), anti–NK1.1-PE-Cy7 (552878, BD Biosciences), anti–granulocyte-differentiation antigen-1-PE-Cy7 (108416, BioLegend), anti–CD4-APC (17-0041-83, eBioscience), anti–major histocompatibility complex II–AF647 (562367, BD Biosciences), anti–CD45-APC-Cy7 (103116, BioLegend), anti–TCRβ-BV711 (563613, BD Biosciences), anti–F4/80-BV421 (123131, BioLegend), or anti–CD8α-PB (558106, BD Biosciences). Cell viability was determined using Zombie AQUA viability dye following the manufacturer's instructions (BioLegend). For intracellular staining of IFN-γ or FOXP3 transcription factor, cells were fixed and permeabilized using the eBioscience Foxp3/Transcription factor staining buffer set (Thermo Fisher Scientific) and incubated with anti–IFN-γ–APC (17-7311-82, eBioscience), anti–FOXP3-PE (12-5773-80, eBioscience), or anti–FOXP3-APC (17-5773-82, eBioscience; both at 1:200), following the manufacturer's protocol. For experiments involving $CCR7^{GFP}$ reporter mice, single-cell suspensions were always acquired fresh and without any fixation step. For experiments involving CCR7 staining ex vivo, single-cell suspensions of dCLNs or meninges were blocked in 50 μl RPMI 1640 with 5% FBS, 10% normal rat serum (STEMCELL technologies), 2% mouse IgG (Jackson ImmunoResearch), and anti-CD16/32 (clone 93) on ice for 15 min. Following the blocking step, 0.5 μg of anti-CD197 (CCR7)–APC (clone 4B12) or rat IgG2a-APC isotype control (clone RTK2758) was added, and cells were incubated at 37°C for 30 min. Cells were washed with PBS and 2% FBS and stained with Zombie NIR fixable viability kit (BioLegend; 1:500) in PBS (without serum) on ice for 20 min. Stained cells were washed with PBS and 2% FBS, followed by incubation with a master mix containing 16 pretitrated concentrations of antibodies in BD Brilliant Plus buffer (BD Biosciences; 1:5) on ice for 30 min: anti–CD4-BUV395 (GK1.5), anti–CD11b-BUV563 (M1/70), anti–CD19-BUV615 (1D3), anti–Ly6G-BUV661 (1A8), anti–CD90.2-BUV737 (53-2.1), anti–TCRβ-BUV805 (H57-597), anti–CD11c-BV421 (HL3), anti–CD24-PB (M1/69), anti–I-A/I-E–BV510 (M5/114.15.2), anti–B220-BV650 (RA3-6B2), anti–CD45-BV750 (30-F11), anti–CD8α–Alexa Fluor 532 (53-6.7), anti–CD3-BB700 (17A2), anti–F4/80-PE (T45-2342), anti–NK1.1-PE-Cy7 (PK136), and anti–Ly6C-APC/Fire-750 (HK1.4). After two washes with PBS and 2% FBS, cells were fixed, permeabilized using the Foxp3 staining buffer set, as described above, blocked with 2% mouse IgG on ice for 15 min, and stained with anti–FOXP3-PE-eF610 (FJK-16s) for 30 min. Fluorescently labeled single-cell suspensions were washed with FACS buffer and acquired in the Gallios Flow Cytometer (Beckman Coulter Inc.) or a Cytek Aurora spectral flow cytometer using SpectroFlo software (Cytek). Acquired data files were unmixed (when applicable), and data analysis was performed using FlowJo 10 software (Becton Dickinson). Briefly, singlets were gated using the height, area, and the pulse width of the forward and side scatters, and then viable leukocytes were selected as $CD45^+$ Zombie $AQUA^-$ ($CD45^+ZA^-$) or Zombie NIR^- ($CD45^+$ $ZNIR^-$). In experiments where brain single-cell suspensions were analyzed, live leukocytes were identified as $CD45^{high}ZA^-$, and live microglia were identified as $CD11b^+CD45^{int}ZA^-$. Cells were then gated for the appropriate cell type markers. An aliquot from the unstained single-cell suspensions was incubated with the ViaStain acridine orange and propidium iodide (AOPI) Staining Solution (CS2-0106, Nexcelom Bioscience) to provide accurate total counts for each sample using Cellometer Auto 2000 (Nexcelom Bioscience). Data processing was performed with Excel, and statistical analysis was performed using Prism 8.3.4.

CyTOF and high-dimensional data analysis

Before the start of the experiment, metal isotope-labeled antibodies were purchased from Fluidigm or conjugated in-house with Maxpar (MP) antibody conjugation kits (Fluidigm) following the manufacturer's protocol. Mice were euthanized and transcardially perfused, skull caps were collected, and brain meninges were harvested and digested to obtain a final single-cell suspension following the same methodology described in the "Flow cytometry" section. Cell suspensions resulting from each brain meninges were transferred in a 96-well plate and washed with MP PBS. An aliquot from the unstained single-cell suspensions was incubated with ViaStain AOPI Staining Solution to provide accurate counts for each sample using Cellometer Auto 2000. Unless stated otherwise, all washes and incubations were performed with MP Cell Staining Buffer. Individual samples were incubated with 50 μl of 2.5 μM cisplatin (Fluidigm) in MP PBS for 5 min at RT, followed by two washes, and preincubated with Fc receptor–blocking solution (anti-CD16/32 in MP PBS supplemented with 0.5% BSA) for 15 min at 4°C. Cells were then stained for fixation-sensitive surface markers for 30 min at 4°C with the following: anti–Ly6C-Nd-142 (clone HK1.4, Maxpar Ready, BioLegend, conjugated in-house), anti–CD169-Sm-147 (clone H1.2F3, Maxpar Ready, conjugated in-house), anti–XCR1-Eu-153 (clone ZET, BioLegend, conjugated in-house), anti–Siglec-H-Gd-160 (clone 551, BioLegend, conjugated in-house), anti–FcER1-Dy-161 (clone MAR-1, Maxpar Ready, conjugated in-house), anti–programmed cell death protein 1 (PD-1)–Er-166 (clone CHBC0116081, R&D Systems, conjugated in-house), anti–H-2Kb/Db-Yb-173 (clone 28-8-6, BioLegend, conjugated in-house), anti–CCR2-FITC (clone 475301, R&D Systems), and anti–Thy1.2-PE (clone 30-H12, eBioscience). After washing twice, cells were fixed in 1.6% PFA in MP PBS for 10 min at RT. Individual samples were barcoded using six palladium metal isotopes according to the manufacturer's instructions (Cell-ID 20-plex Pd barcoding kit, Fluidigm) to reduce tube-to-tube variability. All individual samples were combined in the same tube and subsequently stained as multiplexed samples by incubating for 30 min at RT with the following antibodies: anti–CD45-Yb-89 (clone 30-F11, 3089005B, Fluidigm), anti–CD11b-Nd-143 (clone M1/70, 3143015B, Fluidigm), anti–FITC–Nd-144 (clone FIT22, 3144006B, Fluidigm), anti–CD4-Nd-145 (clone RM4-5, 3145002B, Fluidigm), anti–F4/80-Nd-146 (clone BM8, 3146008B, Fluidigm), anti–Ly6G-Nd-148 (clone 1A8, Maxpar Ready, conjugated in-house), anti–CD19-Sm-149 (clone 6D5, 3149002B, Fluidigm), anti–CD24-Nd-150 (clone M1/69, 3150009B, Fluidigm), anti–CD64-Eu-151 (clone X54-5/7.1, 3151012B, Fluidigm), anti–CD3ε-Sm-152 (clone 145-2C11, 3152004B, Fluidigm), anti–Ter119-Sm-154 (clone Ter119, 3154005B, Fluidigm), anti–PE-Gd-156 (clone PE001, 3156005B, Fluidigm), anti–CD103-Dy-162 (clone FIB504, 3162026B, Fluidigm), anti–CD14-Dy-163 (clone M14-23, Ultra-LEAF, conjugated in-house, BioLegend), anti–CD62L-Dy-164 (clone MEL-14, 3164003B, Fluidigm), anti–CD8α-Er-168 (clone SK1, 3168002B, Fluidigm), anti–TCRβ–Tm-169 (clone H57597, 3169002B, Fluidigm), anti–NK1.1-Er-170 (clone PK136, 3170002B, Fluidigm), anti–CD44-Yb-171 (clone IM7, 3171003B, Fluidigm), anti–CD86-Yb-172 (clone GL1, 3172016B, Fluidigm), anti–I-A/I-E–Yb-174 (clone M5/114.15.2, 3174003B, Fluidigm), anti–CD127-Lu-175 (clone A7R34, 3175006B, Fluidigm), anti–B220-Yb-176 (clone RA3-682, 3176002B, Fluidigm), and anti–CD11c-Bi-209 (clone N418, 3209005B, Fluidigm). The fixed cells were washed and stained for intracellular antigens in the MP Nuclear Antigen Staining Buffer Set (Fluidigm) for additional 30 min at RT with the following: anti–tumor necrosis factor–Pr-141 (clone MP6-XT22, 3141013B, Fluidigm), anti–FOXP3-Gd-158 (clone FJK-16s, 3158003A, Fluidigm) anti–RAR-related orphan receptor gamma delta (RORγδ)-Tb-159 (clone B2D, 3159019B, Fluidigm), anti–T-bet–Ho-165 (clone 4B10, Maxpar Ready, conjugated in-house), and anti–GATA3-Er-167 (clone TWAJ, 3167007A, Fluidigm). Samples were washed twice in Nuclear Antigen Staining Buffer and incubated in 125 nM Ir-191/193 DNA intercalator solution (Cell-ID Intercalator-Ir in Maxpar Fix/Perm buffer, Fluidigm) overnight at 4°C. Before acquisition on a Helios mass cytometer (available at the University of Virginia Flow Cytometry Core Facility), samples were washed twice with MP Fix/Perm buffer, MP water, and MP Cell acquisition solution. Raw data were normalized for detector sensitivity by adding five-element beads to the sample and processed as described previously (*53*). Samples were debarcoded using the Zunder Lab single-cell debarcoder (https://github.com/zunderlab/single-cell-debarcoder) in MATLAB (9.7 version), and files were uploaded in Cytobank (7.2 version). Raw data were subjected to arcsinh transformation (cofactor = 5), manually gated to exclude debris, doublets, dead cells, and normalization beads and include 191/193Ir_DNA$^+$, 195Pt_Cisplatin$^-$, 140Ce_EQbeads$^-$, and 89Yb_CD45$^+$ events that were corrected for Mahalanobis distance. Gating was followed by dimensionality reduction and t-distributed stochastic neighbor embedding–based visualization (viSNE) on the combined dataset. Individual fcs files containing viSNE plots of single live CD45$^+$ events were exported from Cytobank and read into R as a flowset using the flowCore package (R package version 1.48.1). Clustering was performed using the default settings for Rphenograph (Cytofkit package for version 3.5 of Bioconductor) (*54*) and all markers in the panel with the exception of CD45. For the generation of heatmaps showing median marker expression, the median quantile-scaled expression value among cells from each cluster was visualized. Initial Rphenograph nodes depicting the median marker expression values within each cluster were then examined, and clusters were merged to reflect biologically meaningful populations. Initial clustering identified 51 clusters, of which, 8 were identified as CD3$^+$ TCRβ$^+$CD4$^+$ T cells, CD3$^+$TCRβ$^+$CD8$^+$ T cells, or CD3$^+$TCRβ$^+$CD4$^-$CD8$^-$ [double negative (DN)] T cells. viSNE plots showing unsupervised clustering profile of subpopulations of CD45$^+$ live immune cells isolated from the meninges were obtained with 2000 cells that were randomly selected per group. The identified T cell clusters were then subset and reclustered to identify finer resolution populations using FlowSOM with the number of clusters set to 15 (*55*). Further clustering of the T cell subset revealed other negligible contaminating cell populations that were removed from the analysis. After two rounds of reclustering and exclusion, the final T cell subpopulations were defined on the basis of the CD4, CD8, CD103, PD-1, and CD44 phenotypic markers and the FOXP3 and T-bet transcription factors. The frequencies were calculated as the number of cells from each sample belonging to each cluster divided by the total number of T cells subset from that sample. viSNE dimensions were then recalculated using a random sample of 500 cells from each sample. For the generation of heatmaps showing median marker expression, the median quantile-scaled expression value among cells from each cluster was visualized.

Whole-brain blood vascular and myeloid cell sorting

Adult (5 months of age) 5xFAD::CCR7$^{-/-}$ mice, or control age-matched 5xFAD littermates, were euthanized by intraperitoneal injection of Euthasol and transcardially perfused with ice-cold PBS with heparin. The skulls were collected, and the whole brain was carefully dissected into ice-cold advanced Dulbecco's modified Eagle's medium (DMEM)/F12 (12634010, Gibco). Brain tissue was mechanically dissociated with sterile sharp scissors and digested for

45 min at 37°C in advanced DMEM/F12 with collagenase VIII (1 mg/ml), DNase I (50 U/ml), and 1% FBS. Every 15 min, the tissue suspensions were sequentially passed through a 10-ml serological pipette (10 times), followed by two passages through a 5-ml serological pipette (10 times each). Cellular suspensions were filtered through a 70-μm cell strainer, thoroughly mixed with an equal volume of 22% BSA in PBS, and centrifuged at 1000*g* for 10 min at RT (without break), to remove the myelin. After discarding the upper layer and supernatant containing the myelin and cell debris, the cell pellets were washed with advanced DMEM/F12 supplemented with 10% FBS, resuspended in ice-cold FACS buffer, preincubated for 10 min at 4°C with Fc receptor–blocking solution (anti-CD16/32, 101302, BioLegend; 1:200 in ice-cold FACS buffer), and stained for extracellular markers with the following antibodies (at 1:200 in ice-cold FACS buffer, unless stated otherwise): anti–CD13-FITC (558744, BD Biosciences; at 1:50), anti–Ly6G-PE (127608, BioLegend), anti–CD11b PerCP-Cy5.5 (550993, BD Biosciences), anti–CD31-APC (17-0311-80, eBioscience), and anti–CD45-APC-Cy7 (103116, BioLegend). DAPI (0.1 μg/ml) was also added to access cell viability. After an incubation period of 25 min at 4°C, cells were washed and resuspended in ice-cold FACS buffer. Cells were gated on DAPI$^-$ singlets (based on height, area, and the pulse width of the forward and side scatters), CD45$^+$CD11b$^+$Ly6G$^-$ (myeloid cells), and CD45$^-$CD11b$^-$ CD13$^-$CD31$^+$ (BECs) and sorted using the Influx Cell Sorter at the University of Virginia Flow Cytometry Core Facility. The aforementioned enriched single-cell populations pertaining to the same group were sorted into the same 1.5-ml tube previously coated (overnight) with 0.1% ultrapure nonacetylated BSA (AM2616, Thermo Fisher Scientific) in PBS, containing 500 μl of ice-cold advanced DMEM/F12. Single cells were centrifuged at 350*g* for 5 min at 4°C and resuspended in 0.1% ultrapure nonacetylated BSA in PBS at 1000 cells/μl estimated from counting on a hemocytometer and Trypan blue (MilliporeSigma) staining. Single-cell suspensions were kept on ice until further use.

Murine single-cell RNA-seq

For the experiments involving sorted blood vascular and myeloid cells from whole-brain preparations, ~10,000 cells per sample were loaded onto a Chromium Single-Cell A Chip (PN-120236, 10× Genomics) placed in a 10× Chip Holder and run on a 10× platform Chromium Controller to generate complementary DNAs carrying cell- and transcript-specific barcodes. Sequencing libraries were constructed using the Chromium Single-Cell 3′ Library and Gel Bead Kit v2 (PN-120237, 10× Genomics). After a quality control step performed on an Illumina MiSeq Nano system, libraries were sequenced on the Illumina NextSeq platform using paired-end sequencing, with 100,000 reads targeted per cell. All murine single-cell RNA-seq data were generated in the Genome Analysis and Technology Core of the University of Virginia (RRID:SCR_018883). Binary base call (bcl) files were converted to fastq format using the Illumina bcl2fastq2 software. Fastq files were then mapped to the mm10 transcriptome using the CellRanger 3.0.2 pipeline, specifically the count function. The resulting gene by count matrices were then read into R and filtered to remove low-quality cells based on unique molecular counts, unique genes, and percent mitochondrial gene expression. In addition, genes were filtered to retain only those which expressed more than five cells. The remaining cells were then normalized and log-transformed using the scran normalization package (*56*, *57*). The resulting normalized counts were then transformed from $\log_2$ scale to the natural log scale for compatibility with Seurat v3 (*58*), and the effects of sequencing depth per cell, number of unique features, and percentage of mitochondrial genes were regressed out. Highly variable genes were determined using the variance-stabilizing transformation, and the top 2000 most variable genes were used as input for principal components analysis. Principal components were selected on the basis of an elbow plot. On the basis of these results, on the percentage of variance explained by each component and the number of cells in the dataset, the first 10 principal components were used for clustering and t-stochastic neighbor embedding (tSNE) analysis. Cluster membership was determined using shared nearest neighbor graph embedding and optimization of the Louvain algorithm as implemented in the Seurat *FindNeighbors* and *FindClusters* functions with a resolution of 0.8. For cluster markers, the *FindAllMarkers* function was used to test genes showing a minimum log fold change of 0.25 in each cluster versus all other clusters and expressed in a minimum of 30% of cells in the cluster of interest. Cluster annotation was performed manually on the basis of the expression of canonical markers. Cells not of interest to the analysis were removed on the basis of these cluster annotations, including oligodendrocytes, ependymal cells, choroid plexus endothelial cells, a small population of pericytes and smooth muscle cells, and a subcluster of microglia with a similar gene signature to artificially ex vivo activated microglia (*59*). Transcripts were then rescaled, reclustered, and annotated again using the methods described above, and clusters were collapsed on the basis of common cell types. A final number of 8567 cells were obtained, including 1442 arterial BECs, 5181 capillary BECs, 453 venous BECs, 1176 microglia, and 315 BAMs. For analysis of differentially expressed genes between groups, each cluster was filtered to include genes that had at least five transcripts in at least five cells, and then the top 2000 highly variable genes were determined and included for further analysis using the SingleCellExperiment *modelGeneVar* and *getTopHVGs* functions. After filtering, observational weights for each gene were calculated using the ZINB-WaVE *zinbFit* and *zinbwave* functions (*60*). These were then included in the edgeR model, which was created with the *glmFit* function, using the *glmWeightedF* function (*61*). Results were then filtered using as threshold Benjamini-Hochberg adjusted $P < 0.05$ (statistically significant). Volcano plots were made with the EnhancedVolcano package (https://github.com/kevinblighe/EnhancedVolcano). Genes matching this significance threshold were divided on the basis of up- or down-regulation (*62*) and used as input for gene ontology analysis using the ClusterProfiler package (*63*, *64*).

Statistical analysis and reproducibility

Sample sizes were chosen on the basis of standard power calculations (with $\alpha = 0.05$ and a power of 0.8) performed for similar experiments that were previously published (*23*, *25*, *28*). In general, statistical methods were not used to recalculate or predetermine sample sizes. Animals from different cages, but within the same experimental group, were selected to assure randomization. Experimenters were blinded to the identity of experimental groups from the time of euthanasia until the end of data collection and analysis for all the independent experiments. Data showing positive results were confirmed in at least two independent experiments. The Kolmogorov-Smirnov test was used to assess the distribution of the data. Variance was similar within independent groups of the same experiment and between groups from independent experiments. The ROUT and Grubb test were used to identify and discard potential outliers. One outlier was detected and removed in fig. S1 (P to S).

Data in graphs were always presented as means ± SEM. Two-group comparisons were made using two-tailed unpaired Student's *t* test. One-way analysis of variance (ANOVA), with Sidak's or Bonferroni's multiple comparisons tests, was used to compare three independent groups. For comparisons of multiple factors (for example, immune cell type versus treatment), two-way ANOVA with Sidak's multiple comparisons test was used. Repeated-measures two-way ANOVA with Sidak's multiple comparisons test was used to analyze data acquired during the acquisition and reversal of the MWM test. Multiple two-tailed unpaired Student's *t* tests, with two-stage step-up method of Benjamini, Krieger, and Yekutieli and false discovery rate (FDR) (Q) = 0.05, were used for multiple comparisons between two conditions in terms of leukocyte cell cluster number or frequency. Statistical analysis was performed using Prism version 8.3.4.

SUPPLEMENTARY MATERIALS

Supplementary material for this article is available at http://advances.sciencemag.org/cgi/content/full/7/21/eabe4601/DC1

View/request a protocol for this paper from *Bio-protocol*.

REFERENCES AND NOTES

1. M. G. Erkkinen, M. O. Kim, M. D. Geschwind, Clinical neurology and epidemiology of the major neurodegenerative diseases. *Cold Spring Harb. Perspect. Biol.* **10**, (2018).
2. R. Brookmeyer, N. Abdalla, C. H. Kawas, M. M. Corrada, Forecasting the prevalence of preclinical and clinical Alzheimer's disease in the United States. *Alzheimers Dement.* **14**, 121–129 (2018).
3. C. R. Jack Jr., D. A. Bennett, K. Blennow, M. C. Carrillo, B. Dunn, S. B. Haeberlein, D. M. Holtzman, W. Jagust, F. Jessen, J. Karlawish, E. Liu, J. L. Molinuevo, T. Montine, C. Phelps, K. P. Rankin, C. C. Rowe, P. Scheltens, E. Siemers, H. M. Snyder, R. Sperling; Contributors, NIA-AA research framework: Toward a biological definition of Alzheimer's disease. *Alzheimers Dement.* **14**, 535–562 (2018).
4. M. Kivipelto, F. Mangialasche, T. Ngandu, Lifestyle interventions to prevent cognitive impairment, dementia and Alzheimer disease. *Nat. Rev. Neurol.* **14**, 653–666 (2018).
5. F. Panza, M. Lozupone, G. Logroscino, B. P. Imbimbo, A critical appraisal of amyloid-β-targeting therapies for Alzheimer disease. *Nat. Rev. Neurol.* **15**, 73–88 (2019).
6. A. C. Naj, G. Jun, G. W. Beecham, L. S. Wang, B. N. Vardarajan, J. Buros, P. J. Gallins, J. D. Buxbaum, G. P. Jarvik, P. K. Crane, E. B. Larson, T. D. Bird, B. F. Boeve, N. R. Graff-Radford, P. L. De Jager, D. Evans, J. A. Schneider, M. M. Carrasquillo, N. Ertekin-Taner, S. G. Younkin, C. Cruchaga, J. S. Kauwe, P. Nowotny, P. Kramer, J. Hardy, M. J. Huentelman, A. J. Myers, M. M. Barmada, F. Y. Demirci, C. T. Baldwin, R. C. Green, E. Rogaeva, P. S. George-Hyslop, S. E. Arnold, R. Barber, T. Beach, E. H. Bigio, J. D. Bowen, A. Boxer, J. R. Burke, N. J. Cairns, C. S. Carlson, R. M. Carney, S. L. Carroll, H. C. Chui, D. G. Clark, J. Corneveaux, C. W. Cotman, J. L. Cummings, C. DeCarli, S. T. DeKosky, R. Diaz-Arrastia, M. Dick, D. W. Dickson, W. G. Ellis, K. M. Faber, K. B. Fallon, M. R. Farlow, S. Ferris, M. P. Frosch, D. R. Galasko, M. Ganguli, M. Gearing, D. H. Geschwind, B. Ghetti, J. R. Gilbert, S. Gilman, B. Giordani, J. D. Glass, J. H. Growdon, R. L. Hamilton, L. E. Harrell, E. Head, L. S. Honig, C. M. Hulette, B. T. Hyman, G. A. Jicha, L. W. Jin, N. Johnson, J. Karlawish, A. Karydas, J. A. Kaye, R. Kim, E. H. Koo, N. W. Kowall, J. J. Lah, A. I. Levey, A. P. Lieberman, O. L. Lopez, W. J. Mack, D. C. Marson, F. Martiniuk, D. C. Mash, E. Masliah, W. C. McCormick, S. M. McCurry, A. N. McDavid, A. C. McKee, M. Mesulam, B. L. Miller, C. A. Miller, J. W. Miller, J. E. Parisi, D. P. Perl, E. Peskind, R. C. Petersen, W. W. Poon, J. F. Quinn, R. A. Rajbhandary, M. Raskind, B. Reisberg, J. M. Ringman, E. D. Roberson, R. N. Rosenberg, M. Sano, L. S. Schneider, W. Seeley, M. L. Shelanski, M. A. Slifer, C. D. Smith, J. A. Sonnen, S. Spina, R. A. Stern, R. E. Tanzi, J. Q. Trojanowski, J. C. Troncoso, V. M. Van Deerlin, H. V. Vinters, J. P. Vonsattel, S. Weintraub, K. A. Welsh-Bohmer, J. Williamson, R. L. Woltjer, L. B. Cantwell, B. A. Dombroski, D. Beekly, K. L. Lunetta, E. R. Martin, M. I. Kamboh, A. J. Saykin, E. M. Reiman, D. A. Bennett, J. C. Morris, T. J. Montine, A. M. Goate, D. Blacker, D. W. Tsuang, H. Hakonarson, W. A. Kukull, T. M. Foroud, J. L. Haines, R. Mayeux, M. A. Pericak-Vance, L. A. Farrer, G. D. Schellenberg, Common variants at MS4A4/MS4A6E, CD2AP, CD33 and EPHA1 are associated with late-onset Alzheimer's disease. *Nat. Genet.* **43**, 436–441 (2011).
7. R. Guerreiro, A. Wojtas, J. Bras, M. Carrasquillo, E. Rogaeva, E. Majounie, C. Cruchaga, C. Sassi, J. S. Kauwe, S. Younkin, L. Hazrati, J. Collinge, J. Pocock, T. Lashley, J. Williams, J. C. Lambert, P. Amouyel, A. Goate, R. Rademakers, K. Morgan, J. Powell, P. St George-Hyslop, A. Singleton, J. Hardy; Alzheimer Genetic Analysis Group, TREM2 variants in Alzheimer's disease. *N. Engl. J. Med.* **368**, 117–127 (2013).
8. K. Baruch, N. Rosenzweig, A. Kertser, A. Deczkowska, A. M. Sharif, A. Spinrad, A. Tsitsou-Kampeli, A. Sarel, L. Cahalon, M. Schwartz, Breaking immune tolerance by targeting Foxp3$^+$ regulatory T cells mitigates Alzheimer's disease pathology. *Nat. Commun.* **6**, 7967 (2015).
9. Y. Wang, M. Cella, K. Mallinson, J. D. Ulrich, K. L. Young, M. L. Robinette, S. Gilfillan, G. M. Krishnan, S. Sudhakar, B. H. Zinselmeyer, D. M. Holtzman, J. R. Cirrito, M. Colonna, TREM2 lipid sensing sustains the microglial response in an Alzheimer's disease model. *Cell* **160**, 1061–1071 (2015).
10. K. Baruch, A. Deczkowska, N. Rosenzweig, A. Tsitsou-Kampeli, A. M. Sharif, O. Matcovitch-Natan, A. Kertser, E. David, I. Amit, M. Schwartz, PD-1 immune checkpoint blockade reduces pathology and improves memory in mouse models of Alzheimer's disease. *Nat. Med.* **22**, 135–137 (2016).
11. H. Keren-Shaul, A. Spinrad, A. Weiner, O. Matcovitch-Natan, R. Dvir-Szternfeld, T. K. Ulland, E. David, K. Baruch, D. Lara-Astaiso, B. Toth, S. Itzkovitz, M. Colonna, M. Schwartz, I. Amit, A unique microglia type associated with restricting development of Alzheimer's disease. *Cell* **169**, 1276–1290.e17 (2017).
12. S. Krasemann, C. Madore, R. Cialic, C. Baufeld, N. Calcagno, R. El Fatimy, L. Beckers, E. O'Loughlin, Y. Xu, Z. Fanek, D. J. Greco, S. T. Smith, G. Tweet, Z. Humulock, T. Zrzavy, P. Conde-Sanroman, M. Gacias, Z. Weng, H. Chen, E. Tjon, F. Mazaheri, K. Hartmann, A. Madi, J. D. Ulrich, M. Glatzel, A. Worthmann, J. Heeren, B. Budnik, C. Lemere, T. Ikezu, F. L. Heppner, V. Litvak, D. M. Holtzman, H. Lassmann, H. L. Weiner, J. Ochando, C. Haass, O. Butovsky, The TREM2-APOE pathway drives the transcriptional phenotype of dysfunctional microglia in neurodegenerative diseases. *Immunity* **47**, 566–581.e9 (2017).
13. Y. Shi, D. M. Holtzman, Interplay between innate immunity and Alzheimer disease: APOE and TREM2 in the spotlight. *Nat. Rev. Immunol.* **18**, 759–772 (2018).
14. D. Mrdjen, A. Pavlovic, F. J. Hartmann, B. Schreiner, S. G. Utz, B. P. Leung, I. Lelios, F. L. Heppner, J. Kipnis, D. Merkler, M. Greter, B. Becher, High-dimensional single-cell mapping of central nervous system immune cells reveals distinct myeloid subsets in health, aging, and disease. *Immunity* **48**, 599 (2018).
15. Y. Shi, M. Manis, J. Long, K. Wang, P. M. Sullivan, J. Remolina Serrano, R. Hoyle, D. M. Holtzman, Microglia drive APOE-dependent neurodegeneration in a tauopathy mouse model. *J. Exp. Med.* **216**, 2546–2561 (2019).
16. A. J. Filiano, S. P. Gadani, J. Kipnis, How and why do T cells and their derived cytokines affect the injured and healthy brain? *Nat. Rev. Neurosci.* **18**, 375–384 (2017).
17. S. Da Mesquita, Z. Fu, J. Kipnis, The meningeal lymphatic system: A new player in neurophysiology. *Neuron* **100**, 375–388 (2018).
18. K. Alves de Lima, J. Rustenhoven, J. Kipnis, Meningeal immunity and its function in maintenance of the central nervous system in health and disease. *Annu. Rev. Immunol.* **38**, 597–620 (2020).
19. N. C. Derecki, A. N. Cardani, C. H. Yang, K. M. Quinnies, A. Crihfield, K. R. Lynch, J. Kipnis, Regulation of learning and memory by meningeal immunity: A key role for IL-4. *J. Exp. Med.* **207**, 1067–1080 (2010).
20. J. T. Walsh, S. Hendrix, F. Boato, I. Smirnov, J. Zheng, J. R. Lukens, S. Gadani, D. Hechler, G. Golz, K. Rosenberger, T. Kammertons, J. Vogt, C. Vogelaar, V. Siffrin, A. Radjavi, A. Fernandez-Castaneda, A. Gaultier, R. Gold, T. D. Kanneganti, R. Nitsch, F. Zipp, J. Kipnis, MHCII-independent CD4$^+$ T cells protect injured CNS neurons via IL-4. *J. Clin. Invest.* **125**, 699–714 (2015).
21. S. P. Gadani, I. Smirnov, A. T. Smith, C. C. Overall, J. Kipnis, Characterization of meningeal type 2 innate lymphocytes and their response to CNS injury. *J. Exp. Med.* **214**, 285–296 (2017).
22. A. J. Filiano, Y. Xu, N. J. Tustison, R. L. Marsh, W. Baker, I. Smirnov, C. C. Overall, S. P. Gadani, S. D. Turner, Z. Weng, S. N. Peerzade, H. Chen, K. S. Lee, M. M. Scott, M. P. Beenhakker, V. Litvak, J. Kipnis, Unexpected role of interferon-γ in regulating neuronal connectivity and social behaviour. *Nature* **535**, 425–429 (2016).
23. A. Louveau, J. Herz, M. N. Alme, A. F. Salvador, M. Q. Dong, K. E. Viar, S. G. Herod, J. Knopp, J. C. Setliff, A. L. Lupi, S. Da Mesquita, E. L. Frost, A. Gaultier, T. H. Harris, R. Cao, S. Hu, J. R. Lukens, I. Smirnov, C. C. Overall, G. Oliver, J. Kipnis, CNS lymphatic drainage and neuroinflammation are regulated by meningeal lymphatic vasculature. *Nat. Neurosci.* **21**, 1380–1391 (2018).
24. C. F. Vogelaar, S. Mandal, S. Lerch, K. Birkner, J. Birkenstock, U. Buhler, A. Schnatz, C. S. Raine, S. Bittner, J. Vogt, J. Kipnis, R. Nitsch, F. Zipp, Fast direct neuronal signaling via the IL-4 receptor as therapeutic target in neuroinflammation. *Sci. Transl. Med.* **10**, eaao2304 (2018).
25. K. Alves de Lima, J. Rustenhoven, S. Da Mesquita, M. Wall, A. Salvador, I. Smirnov, G. M. Cebinelli, T. Mamuladze, W. Baker, Z. Papadopoulos, B. Lopes, W. Cao, X. Xie, J. Herz, J. Kipnis, Meningeal γδ T cells regulate anxiety-like behavior via IL-17a signaling in neurons. *Nat. Immunol.* **21**, 1421–1429 (2020).
26. A. Louveau, I. Smirnov, T. J. Keyes, J. D. Eccles, S. J. Rouhani, J. D. Peske, N. C. Derecki, D. Castle, J. W. Mandell, K. S. Lee, T. H. Harris, J. Kipnis, Structural and functional features of central nervous system lymphatic vessels. *Nature* **523**, 337–341 (2015).
27. A. Aspelund, S. Antila, S. T. Proulx, T. V. Karlsen, S. Karaman, M. Detmar, H. Wiig, K. Alitalo, A dural lymphatic vascular system that drains brain interstitial fluid and macromolecules. *J. Exp. Med.* **212**, 991–999 (2015).

28. S. Da Mesquita, A. Louveau, A. Vaccari, I. Smirnov, R. C. Cornelison, K. M. Kingsmore, C. Contarino, S. Onengut-Gumuscu, E. Farber, D. Raper, K. E. Viar, R. D. Powell, W. Baker, N. Dabhi, R. Bai, R. Cao, S. Hu, S. S. Rich, J. M. Munson, M. B. Lopes, C. C. Overall, S. T. Acton, J. Kipnis, Functional aspects of meningeal lymphatics in ageing and Alzheimer's disease. *Nature* **560**, 185–191 (2018).
29. A. C. Shaw, D. R. Goldstein, R. R. Montgomery, Age-dependent dysregulation of innate immunity. *Nat. Rev. Immunol.* **13**, 875–887 (2013).
30. J. J. Goronzy, C. M. Weyand, Mechanisms underlying T cell ageing. *Nat. Rev. Immunol.* **19**, 573–583 (2019).
31. S. E. Marsh, E. M. Abud, A. Lakatos, A. Karimzadeh, S. T. Yeung, H. Davtyan, G. M. Fote, L. Lau, J. G. Weinger, T. E. Lane, M. A. Inlay, W. W. Poon, M. Blurton-Jones, The adaptive immune system restrains Alzheimer's disease pathogenesis by modulating microglial function. *Proc. Natl. Acad. Sci. U.S.A.* **113**, E1316–E1325 (2016).
32. C. Spani, T. Suter, R. Derungs, M. T. Ferretti, T. Welt, F. Wirth, C. Gericke, R. M. Nitsch, L. Kulic, Reduced β-amyloid pathology in an APP transgenic mouse model of Alzheimer's disease lacking functional B and T cells. *Acta Neuropathol. Commun.* **3**, 71 (2015).
33. A. Louveau, S. Da Mesquita, J. Kipnis, Lymphatics in neurological disorders: A neuro-lympho-vascular component of multiple sclerosis and Alzheimer's disease? *Neuron* **91**, 957–973 (2016).
34. J. Rustenhoven, A. Drieu, T. Mamuladze, K. Alves de Lima, T. Dykstra, M. Wall, Z. Papadopoulos, M. Kanamori, A. F. Salvador, W. Baker, M. Lemieux, S. Da Mesquita, A. Cugurra, J. Fitzpatrick, S. Sviben, R. Kossina, P. Bayguinov, R. Townsend, I. Smirnov, M. B. Lopes, J. Herz, J. Kipnis, Functional characterization of the dural sinuses as a neuroimmune interface. *Cell* **184**, 1000–1016.e27 (2021).
35. S. Sharma, A. L. Dominguez, J. Lustgarten, High accumulation of T regulatory cells prevents the activation of immune responses in aged animals. *J. Immunol.* **177**, 8348–8355 (2006).
36. J. Kipnis, H. Cohen, M. Cardon, Y. Ziv, M. Schwartz, T cell deficiency leads to cognitive dysfunction: Implications for therapeutic vaccination for schizophrenia and other psychiatric conditions. *Proc. Natl. Acad. Sci. U.S.A.* **101**, 8180–8185 (2004).
37. E. J. Jaehne, B. T. Baune, Effects of chemokine receptor signalling on cognition-like, emotion-like and sociability behaviours of CCR6 and CCR7 knockout mice. *Behav. Brain Res.* **261**, 31–39 (2014).
38. H. Mestre, L. M. Hablitz, A. L. Xavier, W. Feng, W. Zou, T. Pu, H. Monai, G. Murlidharan, R. M. Castellanos Rivera, M. J. Simon, M. M. Pike, V. Pla, T. Du, B. T. Kress, X. Wang, B. A. Plog, A. S. Thrane, I. Lundgaard, Y. Abe, M. Yasui, J. H. Thomas, M. Xiao, H. Hirase, A. Asokan, J. J. Iliff, M. Nedergaard, Aquaporin-4-dependent glymphatic solute transport in the rodent brain. *eLife* **7**, e40070 (2018).
39. J. J. Iliff, M. Wang, Y. Liao, B. A. Plogg, W. Peng, G. A. Gundersen, H. Benveniste, G. E. Vates, R. Deane, S. A. Goldman, E. A. Nagelhus, M. Nedergaard, A paravascular pathway facilitates CSF flow through the brain parenchyma and the clearance of interstitial solutes, including amyloid β. *Sci. Transl. Med.* **4**, 147ra111 (2012).
40. M. V. Guillot-Sestier, K. R. Doty, D. Gate, J. Rodriguez Jr., B. P. Leung, K. Rezai-Zadeh, T. Town, Il10 deficiency rebalances innate immunity to mitigate Alzheimer-like pathology. *Neuron* **85**, 534–548 (2015).
41. P. Chakrabarty, A. Li, C. Ceballos-Diaz, J. A. Eddy, C. C. Funk, B. Moore, N. DiNunno, A. M. Rosario, P. E. Cruz, C. Verbeeck, A. Sacino, S. Nix, C. Janus, N. D. Price, P. Das, T. E. Golde, IL-10 alters immunoproteostasis in APP mice, increasing plaque burden and worsening cognitive behavior. *Neuron* **85**, 519–533 (2015).
42. S. A. Kaeser, M. C. Herzig, J. Coomaraswamy, E. Kilger, M. L. Selenica, D. T. Winkler, M. Staufenbiel, E. Levy, A. Grubb, M. Jucker, Cystatin C modulates cerebral beta-amyloidosis. *Nat. Genet.* **39**, 1437–1439 (2007).
43. V. Stoka, V. Turk, B. Turk, Lysosomal cathepsins and their regulation in aging and neurodegeneration. *Ageing Res. Rev.* **32**, 22–37 (2016).
44. A. Sierksma, A. Lu, R. Mancuso, N. Fattorelli, N. Thrupp, E. Salta, J. Zoco, D. Blum, L. Buee, B. De Strooper, M. Fiers, Novel Alzheimer risk genes determine the microglia response to amyloid-β but not to TAU pathology. *EMBO Mol. Med.* **12**, e10606 (2020).
45. M. Saresella, E. Calabrese, I. Marventano, F. Piancone, A. Gatti, M. G. Calvo, R. Nemni, M. Clerici, PD1 negative and PD1 positive CD4$^+$ T regulatory cells in mild cognitive impairment and Alzheimer's disease. *J. Alzheimers Dis.* **21**, 927–938 (2010).
46. K. Baruch, A. Deczkowska, E. David, J. M. Castellano, O. Miller, A. Kertser, T. Berkutzki, Z. Barnett-Itzhaki, D. Bezalel, T. Wyss-Coray, I. Amit, M. Schwartz, Aging. Aging-induced type I interferon response at the choroid plexus negatively affects brain function. *Science* **346**, 89–93 (2014).
47. N. Rosenzweig, R. Dvir-Szternfeld, A. Tsitsou-Kampeli, H. Keren-Shaul, H. Ben-Yehuda, P. Weill-Raynal, L. Cahalon, A. Kertser, K. Baruch, I. Amit, A. Weiner, M. Schwartz, PD-1/PD-L1 checkpoint blockade harnesses monocyte-derived macrophages to combat cognitive impairment in a tauopathy mouse model. *Nat. Commun.* **10**, 465 (2019).
48. J. C. Cruz Hernandez, O. Bracko, C. J. Kersbergen, V. Muse, M. Haft-Javaherian, M. Berg, L. Park, L. K. Vinarcsik, I. Ivasyk, D. A. Rivera, Y. Kang, M. Cortes-Canteli, M. Peyrounette, V. Doyeux, A. Smith, J. Zhou, G. Otte, J. D. Beverly, E. Davenport, Y. Davit, C. P. Lin, S. Strickland, C. Iadecola, S. Lorthois, N. Nishimura, C. B. Schaffer, Neutrophil adhesion in brain capillaries reduces cortical blood flow and impairs memory function in Alzheimer's disease mouse models. *Nat. Neurosci.* **22**, 413–420 (2019).
49. F. Herisson, V. Frodermann, G. Courties, D. Rohde, Y. Sun, K. Vandoorne, G. R. Wojtkiewicz, G. S. Masson, C. Vinegoni, J. Kim, D. E. Kim, R. Weissleder, F. K. Swirski, M. A. Moskowitz, M. Nahrendorf, Direct vascular channels connect skull bone marrow and the brain surface enabling myeloid cell migration. *Nat. Neurosci.* **21**, 1209–1217 (2018).
50. R. Cai, C. Pan, A. Ghasemigharagoz, M. I. Todorov, B. Forstera, S. Zhao, H. S. Bhatia, A. Parra-Damas, L. Mrowka, D. Theodorou, M. Rempfler, A. L. R. Xavier, B. T. Kress, C. Benakis, H. Steinke, S. Liebscher, I. Bechmann, A. Liesz, B. Menze, M. Kerschensteiner, M. Nedergaard, A. Erturk, Panoptic imaging of transparent mice reveals whole-body neuronal projections and skull-meninges connections. *Nat. Neurosci.* **22**, 317–327 (2019).
51. E. Pasciuto, O. T. Burton, C. P. Roca, V. Lagou, W. D. Rajan, T. Theys, R. Mancuso, R. Y. Tito, L. Kouser, Z. Callaerts-Vegh, A. G. de la Fuente, T. Prezzemolo, L. G. Mascali, A. Brajic, C. E. Whyte, L. Yshii, A. Martinez-Muriana, M. Naughton, A. Young, A. Moudra, P. Lemaitre, S. Poovathingal, J. Raes, B. De Strooper, D. C. Fitzgerald, J. Dooley, A. Liston, Microglia require CD4 T cells to complete the fetal-to-adult transition. *Cell* **182**, 625–640.e24 (2020).
52. N. Habib, C. McCabe, S. Medina, M. Varshavsky, D. Kitsberg, R. Dvir-Szternfeld, G. Green, D. Dionne, L. Nguyen, J. L. Marshall, F. Chen, F. Zhang, T. Kaplan, A. Regev, M. Schwartz, Disease-associated astrocytes in Alzheimer's disease and aging. *Nat. Neurosci.* **23**, 701–706 (2020).
53. R. Finck, E. F. Simonds, A. Jager, S. Krishnaswamy, K. Sachs, W. Fantl, D. Pe'er, G. P. Nolan, S. C. Bendall, Normalization of mass cytometry data with bead standards. *Cytometry A* **83**, 483–494 (2013).
54. J. H. Levine, E. F. Simonds, S. C. Bendall, K. L. Davis, E. D. Amir, M. D. Tadmor, O. Litvin, H. G. Fienberg, A. Jager, E. R. Zunder, R. Finck, A. L. Gedman, I. Radtke, J. R. Downing, D. Pe'er, G. P. Nolan, Data-driven phenotypic dissection of AML reveals progenitor-like cells that correlate with prognosis. *Cell* **162**, 184–197 (2015).
55. S. Van Gassen, B. Callebaut, M. J. Van Helden, B. N. Lambrecht, P. Demeester, T. Dhaene, Y. Saeys, FlowSOM: Using self-organizing maps for visualization and interpretation of cytometry data. *Cytometry A* **87**, 636–645 (2015).
56. D. J. McCarthy, K. R. Campbell, A. T. Lun, Q. F. Wills, Scater: Pre-processing, quality control, normalization and visualization of single-cell RNA-seq data in R. *Bioinformatics* **33**, 1179–1186 (2017).
57. A. T. Lun, K. Bach, J. C. Marioni, Pooling across cells to normalize single-cell RNA sequencing data with many zero counts. *Genome Biol.* **17**, 75 (2016).
58. T. Stuart, A. Butler, P. Hoffman, C. Hafemeister, E. Papalexi, W. M. Mauck III, Y. Hao, M. Stoeckius, P. Smibert, R. Satija, Comprehensive integration of single-cell data. *Cell* **177**, 1888–1902.e21 (2019).
59. S. E. Marsh, T. Kamath, A. J. Walker, L. Dissing-Olesen, T. R. Hammond, A. M. H. Young, A. Abdulraouf, N. Nadaf, C. Dufort, S. Murphy, V. Kozareva, C. Vanderburg, S. Hong, H. Bulstrode, P. J. Hutchinson, D. J. Gaffney, R. J. M. Franklin, E. Z. Macosko, B. Stevens, Single cell sequencing reveals glial specific responses to tissue processing & enzymatic dissociation in mice and humans. bioRxiv 2020.12.03.408542 [**Preprint**]. 3 December 2020. https://doi.org/10.1101/2020.12.03.408542.
60. K. Van den Berge, F. Perraudeau, C. Soneson, M. I. Love, D. Risso, J. P. Vert, M. D. Robinson, S. Dudoit, L. Clement, Observation weights unlock bulk RNA-seq tools for zero inflation and single-cell applications. *Genome Biol.* **19**, 24 (2018).
61. M. D. Robinson, D. J. McCarthy, G. K. Smyth, edgeR: A bioconductor package for differential expression analysis of digital gene expression data. *Bioinformatics* **26**, 139–140 (2010).
62. G. Hong, W. Zhang, H. Li, X. Shen, Z. Guo, Separate enrichment analysis of pathways for up- and downregulated genes. *J. R. Soc. Interface* **11**, 20130950 (2014).
63. G. Yu, L. G. Wang, Y. Han, Q. Y. He, clusterProfiler: An R package for comparing biological themes among gene clusters. *OMICS* **16**, 284–287 (2012).
64. G. Yu, L. G. Wang, G. R. Yan, Q. Y. He, DOSE: An R/bioconductor package for disease ontology semantic and enrichment analysis. *Bioinformatics* **31**, 608–609 (2015).

Acknowledgments: We thank S. Smith for editing the manuscript. We are grateful to S. Blackburn and N. Al-Hamadani for assistance with animal colony maintenance and care. We thank all the members of the Kipnis laboratory and the BIG Center (University of Virginia) for valuable comments during the numerous discussions of this work. **Funding:** This work was supported by grants from the NIH/National Institute on Aging (AG034113 and AG057496) and the Cure Alzheimer's Fund. **Author contributions:** S.D.M. designed and performed all the experiments, analyzed and interpreted the data, and wrote the manuscript. J.H. optimized the CyTOF technique and CCR7 ex vivo staining, performed flow cytometry and CyTOF experiments, analyzed data, and participated in manuscript writing. M.W. helped with CyTOF data analysis and participated in manuscript writing. T.D. performed the single-cell RNA-seq raw data analyses and participated in manuscript writing. K.A.d.L. and G.T.N. assisted in experimental design and assisted during experiments and data analysis. N.D., T.K., and W.B. assisted with experiments, animal genotyping, and blinded data analysis/quantifications. J.K. designed the experiments, provided intellectual contribution, oversaw data analysis and interpretation, and wrote the manuscript. **Competing interests:** J.K. is a member of the scientific advisory group for PureTech. J.K. and S.D.M. hold patents and patent applications related to the findings described here. Other authors declare that they have no other competing interests. **Data and materials availability:** All data needed to evaluate the conclusions in the paper are present in the paper and/or the Supplementary Materials. The new single-cell RNA-seq dataset has been deposited online in the Gene Expression Omnibus (GEO) database under the accession number GSE163725. Custom codes used for analysis of the CyTOF and RNA-seq datasets generated and analyzed in the current study are available from the corresponding authors upon reasonable request. Additional data related to this paper may be requested from the authors.

Submitted 23 August 2020
Accepted 2 April 2021
Published 21 May 2021
10.1126/sciadv.abe4601

Citation: S. Da Mesquita, J. Herz, M. Wall, T. Dykstra, K. A. de Lima, G. T. Norris, N. Dabhi, T. Kennedy, W. Baker, J. Kipnis, Aging-associated deficit in CCR7 is linked to worsened glymphatic function, cognition, neuroinflammation, and β-amyloid pathology. *Sci. Adv.* **7**, eabe4601 (2021).